



A Data-Driven Reduced Order Model for Rotor Optimization

Nicholas Peters^{1,2}, Christopher Silva³, and John Ekaterinaris⁴

¹Aerospace Engineer, NASA Ames Research Center, Moffett Field, CA, USA

²Ph.D. Candidate Aerospace Eng., Embry-Riddle Aeron. Univ., Daytona Beach, FL, USA

³Aerospace Engineer, NASA Ames Research Center, Moffett Field, CA, USA

⁴Prof. Aerospace Eng., Embry-Riddle Aeron. Univ., Daytona Beach, FL, USA

Correspondence: Nicholas Peters, nicholas.j.peters@nasa.gov

Abstract. For rotor design applications, such as wind turbine rotor or Urban Air Mobility (UAM) rotorcraft and flying car design, there is a significant challenge in quickly and accurately modeling rotors operating in complex turbulent flow fields. One potential path for deriving high-fidelity but low-cost rotor performance predictions is available through the application of data-driven surrogate modeling. In this study, an initial investigation is undertaken to apply a proper orthogonal decomposition (POD) based reduced order model (ROM) for predicting rotor distributed loads. The POD ROM was derived based on computational fluid dynamics (CFD) results and utilized to produce distributed pressure predictions on rotor blades subjected to topology change due to variations in twist and taper ratio. Rotor twist, θ , was varied between 0° , 10° , 20° , and 30° while taper ratio, λ , was varied as 1.0, 0.9, 0.8, and 0.7. For a demonstration of the approach, all rotors consisted of a single blade. The POD ROM was validated for three operation cases; a high pitch or a high thrust rotor in hover, a low pitch or a low thrust rotor in hover, and a rotor in forward flight at a low speed resembling wind turbine operation with wind shear. Results showed highly accurate distributed load predictions could be achieved and the resulting surrogate model can predict loads at a minimal computational cost. The computational cost for the hovering blade surface pressure prediction was reduced from 12 hours on 440 cores required for CFD to a fraction of a second on a single core required for POD. For rotor in forward flight cost was reduced from 20 hours on 440 cores to less than a second on a single core. The POD ROM was used to undergo a design optimization of the rotor such that figure of merit was maximized for hovering rotor cases and the lift to drag effective ratio was maximized in forward flight.

1 Introduction

In fields such as wind energy and UAM, it is common practice for the rotor analysis to include fluid-structure interactions, structural dynamics, vehicle component sizing, topology optimization, flight simulation, etc. For each of these tasks, it is essential that there exist a model capable of providing load predictions to a high degree of fidelity for a variety of rotor configurations. One approach to obtaining these load predictions is through mid-fidelity design tools. Over the years, numerous such modeling softwares have been developed. For UAM, examples include Comprehensive Analytical Model of Rotorcraft Aerodynamics and Dynamics (CAMRAD) (Johnson, 1992), Rotorcraft Comprehensive Analysis System (RCAS) (Saber et al., 2004), or Comprehensive Hierarchical Aeromechanics Rotorcraft Model (CHARM) (Quackenbush et al., 1999). Additionally, modeling




25 softwares such as Fatigue, Aerodynamics, Structures, and Turbulence (FAST) (Jonkman and Buhl Jr, 2005), BLADED (DNV, 2018), and HAWC2 (Larsen and Hansen, 2007) have been developed for wind turbine design applications. Through leveraging these analysis tools numerous sub-topics of interest have been investigated ranging from multi-rotor performance prediction (Liew et al., 2020; Conley and Shirazi, 2021) to aeroelasticity (Kecskeny and McNamara, 2016; Yeo et al., 2018). When applied to the early stages of rotor optimization, typically mid-fidelity tools provide an excellent path to identifying a limited design space from which an optimal solution can be obtained. Yet, there still remain significant limitations to mid-fidelity analysis tool sets when applied to rotor operation in complex flow fields. These limitations become particularly pronounced once considering that many UAM rotorcraft will likely have rotors operating in vortex-dominated highly turbulent flow fields, particularly those proposed to operate in multi-rotor configurations or in close proximity to buildings. For wind energy applications, a greater subtopic of concern relates to the optimization of grid layout for wind farms as well as the aeroelastic effects of turbines in yaw. As more rotorcraft and wind turbine designs begin to account for these operating conditions, uncertainty in mid-fidelity tools has led to a broadening of optimal design spaces found in the early stages of the conceptual design process.

One potential solution for narrowing this design space is to apply computational fluid dynamics (CFD). Numerous solvers (mStrand (Lakshminarayan et al., 2017), SU2 (Morelli et al., 2021), OpenFoam (Nuernberg and Tao, 2018), etc.) have been developed to help streamline the process of CFD simulation of rotors. Large Eddy Simulation (LES) (Smagorinsky, 1963) and Detached Eddy Simulations (DES) (Spalart, 1997) studies of isolated rotors have shown to be capable of resolving flow fields relevant for performance and loads of isolated rotors in hover/forward flight (Fitzgibbon et al., 2020), during rotorcraft pitch up maneuvers (Abhishek et al., 2011), and rotor-ship wake interactions (Crozon et al., 2018). In a recent publication by Sood et al. (2022), high-fidelity LES simulations were completed for five different inflow conditions of the Lillgrund wind farm. Close comparisons were then drawn between CFD computations and field measurements for turbine power production, loading, and wake recovery. However, for engineering tasks that require hundreds if not thousands of iterations such as design optimization full CFD modeling is not a viable option. Despite significant advancements in both the hardware (Chau, 2019) and software (Wang and Zhai, 2016) rotorcraft CFD simulations still remain too computationally expensive for many engineering tasks. For a detailed comprehensive CFD analysis of a full-scale rotorcraft or wind turbine, computational expense commonly requires simulation on large cluster computers with run times ranging from days to weeks (Neerarambam et al., 2021). It is this resource and time limitation that has led to a desire for devising CFD-based surrogate models.

While currently available computational resources limit the number of CFD simulations during conceptual design to a few tens of runs, recent studies have shown that by retaining a truncated subset of dominate flow features a useful and meaningful reduced order model (ROM) can be constructed (Colella et al., 2021; Liu et al., 2021). In a recent example from Sengers et al. (2022), LES simulations were first completed for a single isolated turbine where rotor configuration was modeled numerically with an actuator disk. Simulations were completed while varying inflow conditions into the actuator disk. Solutions from these LES simulations were leveraged to construct a ROM which mapped inflow conditions to overall normalized wake center deficit, vertical position with respect to hub height, and vertical extension of the wake. A comparison of the ROM to new LES simulations showed ROM was capable of producing accurate predictions for parametric definitions of the turbine's wake. Yet, while such a ROM may be useful for optimizing grid layout of wind farms, for the design optimization of the rotor itself greater



60 emphasis must be placed on achieving an accurate representation of the rotor's surface load distribution. Such a ROM would
 w for the consideration of peak rotor loading, rotor radial loading, rotor stall, etc. all in the earliest stages of the rotor design
process.

As such, in this study, an example of a ROM-based surrogate model for distributed surface loading on rotors will be pre-
sented. This ROM was constructed in a two-step process. First, a low rank subspace is identified. This subspace can be found
65 using a variety of modal decomposition methods such as Proper Orthogonal Decomposition (POD), Dynamic Mode Decom-
position (DMD) (Schmid, 2010), Spectral Proper Orthogonal Decomposition (SPOD) (Sieber et al., 2016), etc. These methods
are all based on the assumption that the flow field of interest can be decomposed to a limited set of dominant characteristics
(Ma et al., 2000). In the present work, the POD algorithm was utilized to identify a low rank subspace. Once a subspace was
identified an interpolation scheme is then applied to make predictions. Recent work has shown that these ROM-based surrogate
70 models are able to retain a high degree of fidelity while operating at a minimal computational cost. Examples of areas of ROM
application include heat transfer (Chen et al., 2015), combustion (Chang et al., 2019), turbine blade modeling (Jin et al., 2017),
boundary layer ingestion (Cinquegrana and Vitagliano, 2021), and store separation (Peters et al., 2021, 2022a, b).

While previous studies have applied POD, DMD, or NN based ROMs to isolated bodies and airfoils with varying inflow con-
ditions, there have been few demonstrations to modeling surface pressure distributions for three-dimensional moving bodies,
75 particularly once variation in surface topology is considered. A significant contributing factor for this absence of literature is
that data-driven modeling relies heavily on the assumption that dominant physics for the system of interest are comprehensively
captured in the training dataset. For this reason, many applications of CFD based data-driven ROMs, while valuable demon-
strations rely on either two-dimensional flows (airfoil load prediction (Yonekura and Suzuki, 2021)), steady-state assumptions
(supersonic flows (Dreyer et al., 2021)), or systems where symmetry/periodicity boundary conditions can be leveraged (rotor-
80 stator modeling (Cizmas and Palacios, 2003)) such that CFD computational expense is minimized and the number of sample
points can be maximized. For rotorcraft applications of CFD based data-driven ROMs, whether they be POD, DMD, or even
neural network (NN) based, the computational expense is comparatively large resulting in a minimal sampling of the domain.
As such, the POD ROMs demonstrated in this study will need to extract meaningful information from a relatively small number
of samples.

85 Typically, there are two ways in which a parametric interpolation based POD ROM could fail to produce meaningful predic-
tions. The first potential situation could be through the POD algorithm being incapable of representing the space with a limited
expansion of modes. Ultimately POD mode retention could be expanded to several hundreds of modes. However, this high
mode count often results in more challenging interpolations. Typically, while initial POD modes can smoothly be correlated
to design parameters, higher mode numbers are often more stochastic resulting in more challenging interpolations. The other
90 way a POD ROM may fail to provide accurate predictions is through under-sampling a sufficiently non-linear design space. If
a design space is found to be highly non-linear, then the total number of CFD simulations required to derive a model may no
longer warrant or even justify the construction of a ROM. Analogous limitations exist for DMD and NN which often require
very large data sets for training and significant computing resources. However, ROMs based on DMD, POD, or NN possess
similar accuracy in reproducing CFD data (Peters et al., 2022c; Raissi et al., 2019).



95 To investigate POD ROM capability in the field of rotor pressure load predictions, a POD ROM was derived and tested
under three operating conditions for a single, isolated blade. The isolated blade was chosen in order to replicate wind turbine
or helicopter rotor operation at a reasonable computational cost. Isolated rotor blades however have been employed in both
experimental (Ramasamy et al., 2009) and theoretical studies for detailed investigation of characteristic features such as the
tip vortex. With each demonstration case, design space complexity was increased to test POD ROM reconstruction and in-
100 terpolation capability. In each scenario, the rotor blade's taper ratio and twist were varied to construct 16 CFD simulations
using the OVERFLOW solver (Buning et al., 1988). A POD ROM was constructed from these cases, validated against three
additional combinations of taper and twist, and then employed to achieve a design optimization of the rotor blade. In this work,
for hovering rotor demonstration cases figure of merit and slices for the coefficient of pressure at the $r/R = 0.95$ radial station
of the blade will be used as metrics for ROM prediction accuracy. For the forward flight demonstration case, both lift to drag
105 effective ratio and integrated sectional coefficients of thrust are used as the metric for ROM prediction accuracy. With these
three ROMs, the study aims to provide insight into the capabilities of POD ROMs for distributed load predictions and rotor
performance prediction given a variation in blade topology over a variety of standard rotor operating conditions.

The rest of this paper is organized as follows. The CFD simulation case setup, grid generation methods, and optimization
algorithm are all outlined in the Numerical Approach section first. The ROM Approach section then overviews the modal
110 decomposition and interpolation schemes used in this work. The Results and Discussion section provides an overview of
the study's findings. Results are split between hovering rotor and forward flight demonstration cases. In the final section,
Conclusions and Outlook, closing remarks are summarized along with future applications of work.

2 Numerical Approach

Before this study could begin, a procedure was required for efficiently generating rotor blade grids given a linear variation in
115 the parameters of taper ratio and twist. This procedure was necessary not only for generating grids for CFD simulation but
also for applying POD ROM for iterative design optimization. As such, a procedure was developed over the course of this
study which allows for a parametric definition of rotor blades. The procedure starts by reading a single input file that holds the
definition of rotor blade's twist (θ), taper (λ), sweep, dihedral, and airfoil cross-section at a number of span-wise stations. These
input file formats can either be obtained from National Aeronautics and Space Administration (NASA) Design and Analysis
120 of Rotorcraft (NDARC) (Johnson, 2015) geometry files or from CAMRAD. A PLOT3D (Walatka, 1990) file is then generated
for the rotor's Cartesian surface grid. With the meshing algorithm defined, the study began generating the 16 blades, as defined
in Table 1 and 3 validation grids, as outlined in Table 2. Each blade consisted of 276 chord-wise and 128 span-wise nodes for
a total surface cell count of 34,944. All 16 blades had a mean chord of 1 ft and a radius of $R = 10$ ft. Examples of blades from
cases **c1** and **c16** can be seen in Fig. 1.

125 Each rotor was limited to a single blade to simplify rotor geometry and limit the influence of variables not represented in the
POD ROM from affecting blade pressure distributions. It should be noted that this geometric constraint is not consistent with
blade counts found on rotorcraft and thus typical rotor performance for UAM aircraft may not be represented in the current

study. Nonetheless, this geometric constraint still allows for pressure distributions representative of those found for blades in hover and forward flight to be modeled thus allowing the study to efficiently identify a POD ROMs applicability to the field of rotorcraft engineering. The selected geometries produce a constrained domain within which a POD ROM can be tested for ability to reconstruct typical load distributions found on blades and model their evolution as a blade's twist and taper ratio varies.

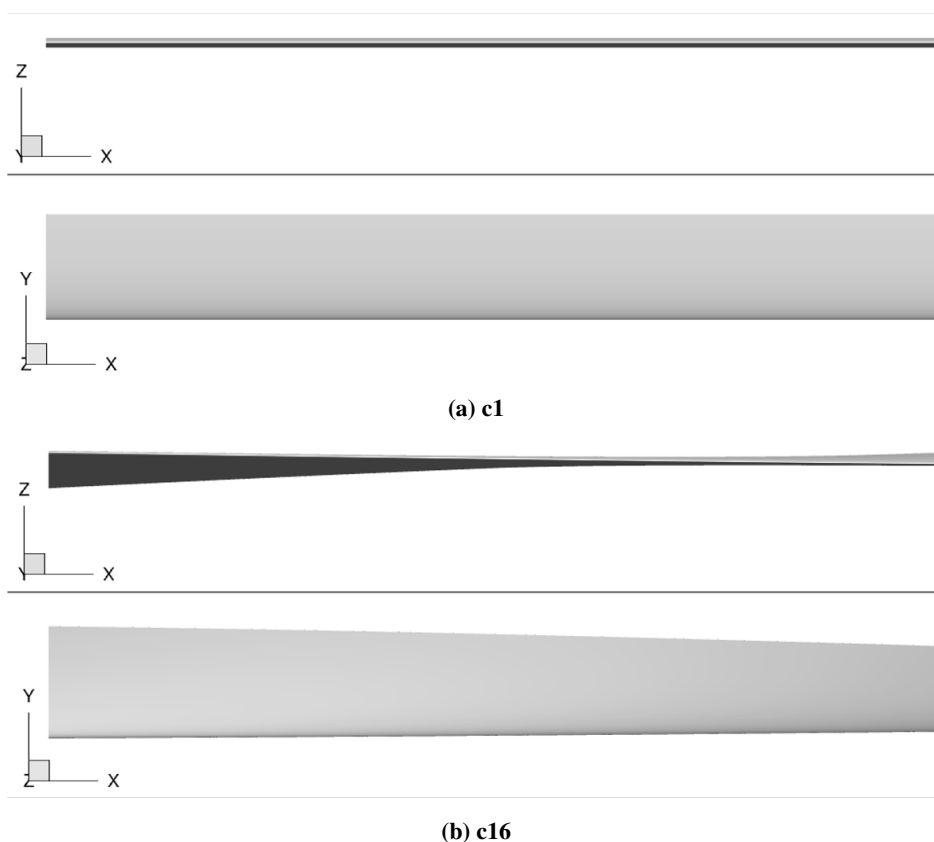


Figure 1. Comparison of two geometries used in this study. Image (a) shows $\theta = 0^\circ$ & $\lambda = 1.0$. Image (b) shows $\theta = 2^\circ$ & $\lambda = 0.7$.

To generate closed surfaces for the rotor's root and tip faces, the Chimera Grid Tools' (CGT's) WINGCAP software was used (Chan, 2005; Rogers et al., 1998). The CGT is a tool-set developed by NASA for the purpose of pre- and post-processing of chimera overset grids (Benek et al., 1986), particularly for use in NASA's OVERFLOW CFD solver. Volume grids were generated from the surface meshes using CGT's hyperbolic grid generator HYPGEN (Chan and Buning, 1993) software. An example of the HYPGEN generated extrusion is shown in Fig. 2. Total near body volume cell count for each case is 3.5 million. Normal spacing at the surface was at a y^+ of 1 and growth was limited to a rate of 1.2. A Cartesian background mesh was then constructed with pressure farfield boundary conditions extending 15 rotor radii from origin. The SAMcart solver was used for the background mesh.

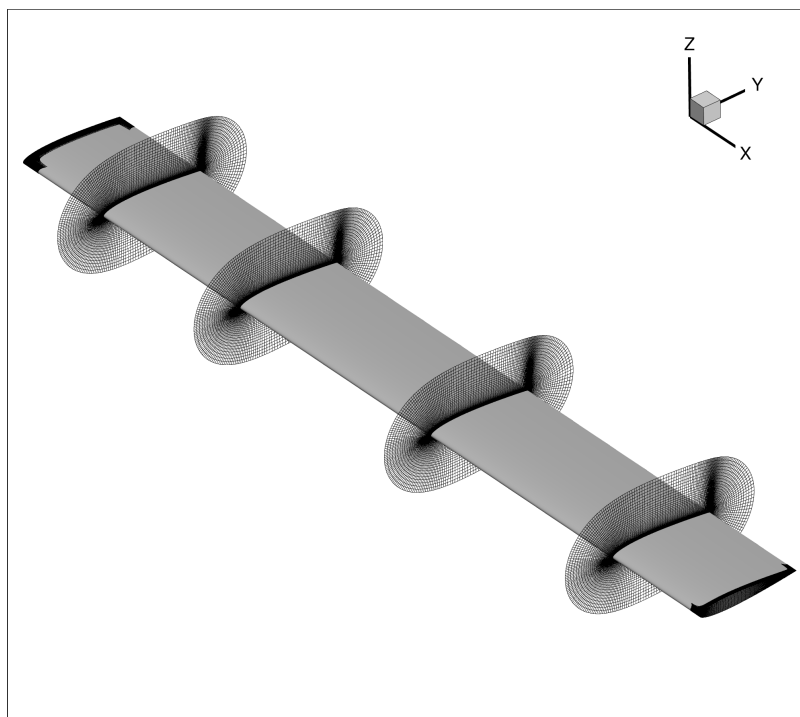


Figure 2. Example of blade volume mesh generated for rotor geometry **c1** shown as slices of volume mesh at radial positions of $x/R = 0.30$, 0.57 , and 0.86 . Surface grids generated for rotor tip and root faces are additionally depicted.

For numerical simulation, the OVERFLOW CFD solver was used. OVERFLOW was developed by NASA and uses a series of structured, overset grids to model fluid flows. For turbulence modeling, the one equation Spalart-Allmaras model was used with curvature corrections (Spalart and Allmaras, 1992). Second order temporal and spatial accuracy was used. To assist in case setup, the CREATE-AV Helios modeling tool was used (Wissink et al., 2016; Sankaran et al., 2010). The Helios code takes a modular approach to numerical simulation where users are allowed to interchange meshing and solver algorithms and thus allows for a broader flexibility for the code to be applied to a variety of topics (Wissink et al., 2018; Anusonti-Inthra, 2018; Ho et al., 2019). For the hovering rotor cases, 5 startup revolutions were completed before extracting rotor surface pressures. For the forward flight cases 8 rotor revolutions were completed before extracting rotor surface pressures. Startup revolutions were selected such that periodic solutions were obtained. Clearly, because of these requirements the cost of the CFD simulations is high. Each forward flight CFD simulation required 12 hours to compute on 440 cores.

For the high thrust hovering rotor, 16 CFD simulations covering geometries outlined in Table 1, were completed with a fixed collective of 8° . These cases were used to construct the first POD-ROM. This ROM was then validated against the three additional validation rotor geometries outlined in Table 2. For the low thrust hovering rotor, CFD simulations were again completed covering geometries outlined in Table 1 with a fixed collective of 4° . A POD ROM-based surrogate model was constructed and validated for all three validation geometries. For rotor in forward flight the same simulations were completed



with a fixed collective of 4° and free stream flow of $M = 0.1$ moving in the positive x-axis direction. For all CFD simulations a tip Mach number of $M_{tip} = 0.5$ was used. For this study, no cyclic pitching or flapping motion was prescribed for the blade. Additionally, the rotor is not trimmed for the balancing of forces or moments, and all rotors are considered to be rigid rotors.

Table 1. The 16 geometries used for derivation of POD-ROM in both hover and forward flight.

		Twist(deg) θ			
		0°	10°	20°	30°
Taper Ratio λ	1.0	<i>c1</i>	<i>c2</i>	<i>c3</i>	<i>c4</i>
	0.9	<i>c5</i>	<i>c6</i>	<i>c7</i>	<i>c8</i>
	0.8	<i>c9</i>	<i>c10</i>	<i>c11</i>	<i>c12</i>
	0.7	<i>c13</i>	<i>c14</i>	<i>c15</i>	<i>c16</i>

Table 2. The 3 geometries used for validation of POD-ROM in both hover and forward flight.

Geometries	Twist (deg)	Taper
<i>v1</i>	15°	1.0
<i>v2</i>	0°	0.85
<i>v3</i>	15°	0.85

The surrogate model based on POD ROM was subsequently used to optimize the blade's twist and taper ratio such that either hovering figure of merit (FM) or forward flight lift to drag effective ratio (L/De) would be maximized. To undergo this optimization, three blade surface grids were first generated. The first grid was generated using the current iteration's solution for optimal twist and taper ratio. Two additional grids were then generated, the first used a 0.1% increase in twist while the second used a 0.1% increase in taper ratio. Solutions for distributed pressures were obtained using the derived POD ROM from which loads were integrated and used to solve for either FM or L/De of each blade. First derivatives for either FM or L/De with respect twist and taper ratio were solved using a first order Euler approximation and used to select new optimal twist and taper ratio through the usage of steepest descent algorithm. A criterion of 0.1% change in solution was selected as a stopping condition.

In this study, FM was computed using Eq. 1. To compute both coefficient of thrust, C_T , and coefficient of torque, C_Q , blade distributed surface pressure solutions were numerically integrated. For rotor in forward flight, integrated sectional coefficients of thrust were plotted from azimuth 0° to 360° . While viscous CFD solutions were obtained in this study, shear stresses were not utilized when computing integrated loads for either POD ROM or CFD. Given that the objective of this study was to



provide an initial investigation of POD ROM distributed load prediction capability for rotor blades, expanding POD ROM to include multi-directional shear loads was not warranted in the current work.

$$FM = \frac{C_T^{3/2}}{C_Q \sqrt{2.0}} \quad (1)$$

175 For the rotor in forward flight cases, L/De was computed by first integrating distributed pressure loads for mean rotor lift L during the blades rotation. Distributed pressure loads were then integrated to find mean power P required by rotor during blades rotation. Once again, viscous loads were not utilized when computing integrated loads for either the POD ROM or CFD predictions. The formulation used to compute L/De is shown in Eq. 2 where v is forward velocity.

$$L/De = \frac{Lv}{P} \quad (2)$$

180 3 ROM Approach

In this section, the methodology used for ROM-based surrogate model construction will be outlined. The method used in this study consisted of two steps. The modal decomposition method will be reviewed first. Next, the interpolation approach used in this study to construct the surrogate model from the ROM POD modes will be reviewed.

3.1 Proper Orthogonal Decomposition

185 The POD was introduced as a method for extracting a low dimensional subspace which captures the majority of the variance, often referred to as energy, from the full phase space (Holmes et al., 1996). While there exist numerous formulations for POD, in this paper the snapshot method as introduced by Sirovitch (Sirovich, 1987) will be used. In this approach any scalar of the flow field can be represented by the sum of the scalar's time-average, $\bar{\mathbf{u}}(\mathbf{x})$, and n orthonormal POD modes $\Phi_i(\mathbf{x})$ times the temporal coefficient $\mathbf{a}_i(t)$. In this study, surface pressure solutions were used to formulate the snapshot matrix. The relationship
 190 is shown below, where $\mathbf{a}_i(t) = \langle (\mathbf{u}(\mathbf{x}, t) - \bar{\mathbf{u}}(\mathbf{x})), \Phi_i^T(\mathbf{x}) \rangle$.

$$\mathbf{u}(\mathbf{x}, t) = \bar{\mathbf{u}}(\mathbf{x}) + \sum_{i=1}^n \mathbf{a}_i(t) \Phi_i(\mathbf{x}) \quad (3)$$

To obtain $\Phi_i(\mathbf{x})$ the a snapshot matrix $\mathbf{u}(\mathbf{x}, t)$ is first formed. In this matrix, the row space holds spatial information while the column space holds temporal information. The perturbation matrix, $\mathbf{u}(\mathbf{x}, t)'$, is calculated by subtracting out the snapshot matrix's time-average. The POD modes are then found through a single value decomposition (SVD) of $\mathbf{u}(\mathbf{x}, t)'$, where the
 195 subset of modes Φ_i are extracted from \mathbf{U} . In Eq. 4, \mathbf{U} contains the eigenvectors for $\mathbf{u}(\mathbf{x}, t)'$ times its transpose, \mathbf{V}^T contains the eigenvectors of the transpose of $\mathbf{u}(\mathbf{x}, t)'$ times itself and Σ contains the singular values of the SVD.

$$\mathbf{u}(\mathbf{x}, t)' = \mathbf{U} \Sigma \mathbf{V}^T \quad (4)$$



The process of reducing the dimensionality of the data-set down to a low rank subspace has been described in numerous publications (Brunton and Kutz, 2019; Holmes et al., 1996). For the present study, the process of selecting an adequate subspace was based on energy retention. For this approach, the number of modes which must be retained is dependent on the behavior of the singular values, s , found in the diagonal of the Σ matrix. Given that s is little more than the square of the eigenvalues of $\langle \mathbf{u}(\mathbf{x}, t)', \mathbf{u}(\mathbf{x}, t)'^T \rangle$, this then serves as a representation for how much of the snapshot matrix's energy, E , is being captured by each mode. The amount of energy being captured in each mode can then be visualized by plotting the ratio of each singular value s_i to the sum of s denoted at \tilde{s} . The objective is then to retain a subset of modes, n , such that Eq. 5 is satisfied.

$$E = \sum_{i=1}^n \frac{s_i}{\tilde{s}} \quad (5)$$

Once a POD model of the form of Eq. 3 had been constructed for the surface loads of various cases, an interpolation scheme is needed in order to make use of these modes for intermediate case predictions.

3.2 2-D Surface Map Interpolation

In order to produce a continuous representation of the temporal coefficients a two-dimensional mapping was constructed. During the construction of these mappings, the objective was to produce a continuous representation for the temporal coefficients. This continuous representation was provided by relating twist θ and taper ratio λ to the temporal coefficients $\mathbf{a}_i(t)$.

$$\mathbf{a}_i(t) = F(\lambda, \theta) \quad (6)$$

Note that for the 2-D surface mapping method, it is an inherent requirement that the two variables selected combine to produce a unique definition of each snapshot. In the case of this study, selection of interpolation parameters becomes trivial. By selecting λ and θ as the mapping variables, any location on the snapshot matrix could be uniquely identified and a spline surface could be fit for each mode temporal coefficients. The advantage is that this method is relatively simple, accurate, and computationally inexpensive to setup. There is no training requirement as in neural networks, or large matrix inversions to make, and the user has a much greater degree of control over how the mapping can be constructed — whether a polynomial, linear, or logarithmic fit depending on the prior knowledge of the problem in hand.

4 Results and Discussion

In this section, the results for CFD simulation, the POD ROM reconstruction, and necessary validations of the ROM and surrogate models will be presented. Results are primarily split between the hovering and forward flight demonstration cases. These two sections will be further split into three additional sections showing CFD simulation results, POD ROM reconstruction results, and POD ROM validation results.



225 4.1 Hovering Rotor Cases

In the first two scenarios of POD ROM rotor blade modeling, an isolated rotor blade in hovering conditions is used. With these two demonstration cases, the study was able to first test for the most basic operating conditions of which a rotorcraft-based POD ROM would be required to model. For an isolated rotor blade in hover after the initial transients are removed time variance can be neglected and thus the focus of the analysis is limited to POD ROM capability for accuracy of both reconstruction and prediction of the spatial characteristics of the domain. This truncation of the time domain leads to the additional advantage of minimizing the size of the snapshot matrix required for the POD ROM to model. As opposed to time-varying systems, such as rotor in forward flight, where numerous snapshots are required per sampling point of the domain to accurately capture the time dynamics of each CFD simulation, for the hovering rotor only a single snapshot is required per sampling point. This relatively small snapshot matrix both minimizes the computational expense of deriving the POD ROM and helps to limit information content in the system thus maximizing the ability of each POD mode to retain a high percentage of the total energy.

By reducing rotor collective to vary between high and low thrust hovering rotor scenarios there is an overall increase in design space non-linearity and spatial information complexity within the domain. In this demonstration case, the influence this increased complexity has on POD ROM capability to both replicate and predict rotor load distributions are investigated. Evidence for the increased complexity of spatial information can be found when comparing rotor pressure distributions between high and low thrust configurations. For the high thrust case, the rotor's wake is convected downstream rapidly. This results in the rotor wake having a smaller degree of influence on the overall rotor pressure distributions. The coefficients of pressure were taken at the $r/R = 0.95$ radial station on the rotor for case **c4** ($\lambda = 1.0$, $\theta = 30^\circ$) and are plotted in Fig. 3 (a) to demonstrate the largely smooth variations in surface pressure of the blade. These relatively small gradients in surface pressure typically result in smaller POD mode retention counts required to comprehensively represent the system.

This is in contrast to the low thrust hovering cases where distributed loads vary to a larger degree in the spanwise direction, particularly at the rotor's tip, caused by the blade's wake being convected away at a slower rate. As a result, there is a significant increase in tip wake interactions with the rotor's pressure distribution. Results for low thrust hovering rotor coefficients of pressure at the $r/R = 0.95$ radial station for case **c4** ($\lambda = 1.0$, $\theta = 30^\circ$) are plotted in Fig. 3 (b). These results demonstrate that non-linearity on coefficients of pressure distributions at the $r/R = 0.95$ radial station has increased.

This increase in complexity may lead to a significant modeling challenge for POD-based surrogate ROMs. As more spatial information is introduced into the domain, energy content may become distributed over a larger range of POD modes. Yet, for an interpolation-based surrogate POD ROM to make accurate predictions of a domain a limited number of POD modes should be retained. While initial POD modes can typically be related well to parameters of interest of the domain, modes associated with higher mode counts tend to be stochastic making derivation of meaningful interpolation models rigorous. Thus, by applying the POD ROM to both high and low thrust hovering cases the study investigates the influence this increased spatial complexity has on the capability of the POD ROM to replicate the domain with a minimal POD mode retention count.

An alternative approach to distributed pressure load modeling could be to avoid modal decomposition methods altogether and deploy a kernel-based learning method in the form of a convolutional neural network (CNN). A significant advantage

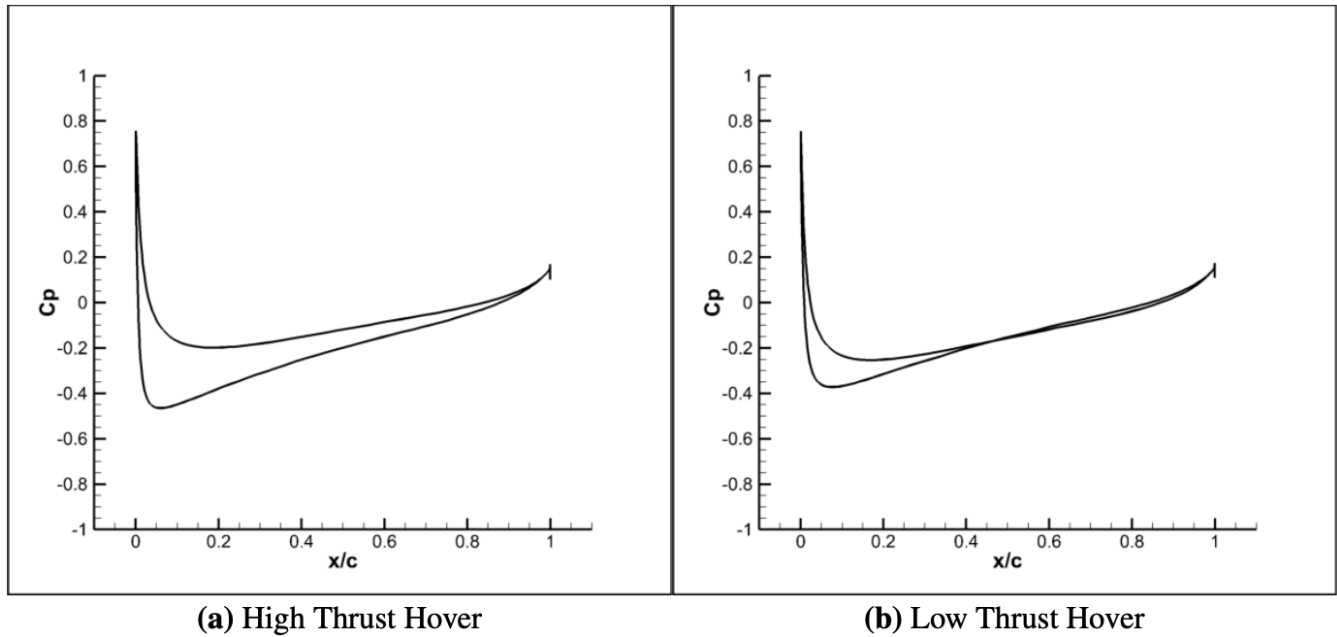


Figure 3. Coefficients of pressure at $r/R=0.95$ as computed through CFD for both high thrust hover (a) and low thrust hover (b). Comparison is shown for sample geometry **c4**.

CNN models have over POD models is their ability to extract features from a data set at various scales and translations. Once a
260 flow feature is identified, such as either rotor vortex rings (Abrams, Jennifer and Hariharan, Nathan S, 2022) or shockwaves (Liu
et al., 2019), the feature can be either identified or replicated at various positions and scales within the domain of interest with
minimal computational effort. Given these characteristics, CNNs have historically shown relatively few limitations in their
capability to replicate training data sets in comparison to modal decomposition-based methods.

However, while CNNs have shown an enhanced capability to extract meaningful features from complex data-sets, there
265 exist significant challenges in deriving a network capable of utilizing these features for meaningful predictions. This chal-
lenge becomes particularly pronounced when deriving CNN models from a sparse sampling of the domain. Typically, to learn
meaningful relationships between parameters of interest and the dynamics of the domain a sufficiently large sampling of the
domain must be obtained. Such large sampling may be possible in the case of either two-dimensional or three-dimensional
steady-state CFD simulations. Yet, for unsteady three-dimensional CFD simulations with multi-body motion, as is required
270 for UAM rotorcraft CFD modeling, computational expense greatly limits the capability to obtain the required sampling of a
domain. Additionally, there is also a significant computational expense associated with deriving CNN models compared to
POD models. Both hovering rotor POD ROMs were derived in less than a second of computing time. Meanwhile, a CNN
derived by the study for a similar rotor performance prediction application required over twelve hours of computing time de-
spite being deployed to a graphical processing unit (GPU). Given the limited domain sampling capability associated with CFD



275 simulations of the UAM field and significant computational expense associated with deriving CNNs, the application of ROM modeling techniques for UAM rotorcraft at present remains largely limited to modal decomposition-based methods.

In addition to an increase in complexity of the surface pressure distribution, there is a significant influence the rotor collective has on the range of load distributions within the design space. When observing surface plots for the integrated figure of merit (FM) of both high and low thrust demonstration cases, Fig. 4, a series of key observations can be drawn. First and foremost is the increased range of FM , and thus increased range of pressure distributions, the POD ROM is required to model. For the rotor in high thrust hover FM varies from 0.65 to 0.73. Yet, by decreasing rotor collective the range of FM for the low thrust hovering rotor nearly doubles resulting in FM varying from 0.45 to 0.67. Note, the minimums and maximums for the domains are found from the sparse CFD simulation sampling of the domain and may not necessarily reflect true local optimal solutions of the respective domains.

285 Based on the limited number of CFD runs (16 for each case), Fig. 4 also demonstrates how reducing rotor collective can lead to an increase in design space non-linearity. In Fig. 4 (a), gradients of FM with respect to θ and λ are shown to be minimal. The FM is shown to have a near-uniform decrease radially from the local optimal in the design space thus resulting in a largely linear relationship between FM and the rotors λ and θ . For the high thrust rotor maximum FM can continuously be found near $\theta = 20^\circ$ as λ goes from $\lambda = 1.0$ to $\lambda = 0.7$. For high thrust hovering rotor, local optimal of $FM = 0.7307$ is found at $\lambda =$
290 1.0 and $\theta = 20^\circ$ through sparse sampling of the domain with CFD simulation.

As collective is decreased for the low thrust rotor FM , Fig. 4 (b), FM is shown to be both varying non-uniformly radially from the local optimal and have a varying local optimal θ as λ goes from 1.0 to 0.7. When $\lambda = 1.0$ local optimal θ is found to be around $\theta = 10^\circ$ while $\lambda = 0.7$ results in a local optimal twist of $\theta = 30^\circ$. Thus, λ and θ are shown to have varying, non-linear influences over the domain of interest. While this increase in non-linearity will not lead to deterioration in the reconstruction capabilities of POD ROM, as it does not necessarily produce more complex spatial information, it will ultimately create a more challenging modeling requirement for POD ROM to produce accurate distributed load predictions. The characteristic of having multiple variables with widely varying degrees of influence on the system is commonplace for many practical rotorcraft applications including hysteresis modeling, aeroelasticity, controls, etc. If a multi-variable data-driven model is to be successfully derived for rotorcraft applications it must be capable of efficiently extracting the relationship each design variable has with rotor surface loads, whether that relationship is linear, quadratic, logarithmic, etc. For low thrust hovering rotor, local optimal of $FM = 0.6675$ is found at $\lambda = 1.0$ and $\theta = 10^\circ$ through sparse sampling of the domain with CFD simulation.

4.1.1 Hovering ROM Reconstruction

After completing all 16 high thrust hovering rotor CFD simulations, solutions for surface pressure were compiled to form a single snapshot matrix. The POD algorithm was then used on this snapshot matrix after which an energy retention criteria was prescribed as outlined in Eq. 5. Percent energy retention per POD mode retention count can be found in Fig. 5 (a). Given the limited number of snapshots used to define to design space, and thus increased ability for POD modes to retain energy, a relatively large energy retention criteria of 99.9% was set after which it was determined that only 8 POD modes were required to produce the desired energy retention. This procedure was then repeated for the low thrust rotor demonstration case and results

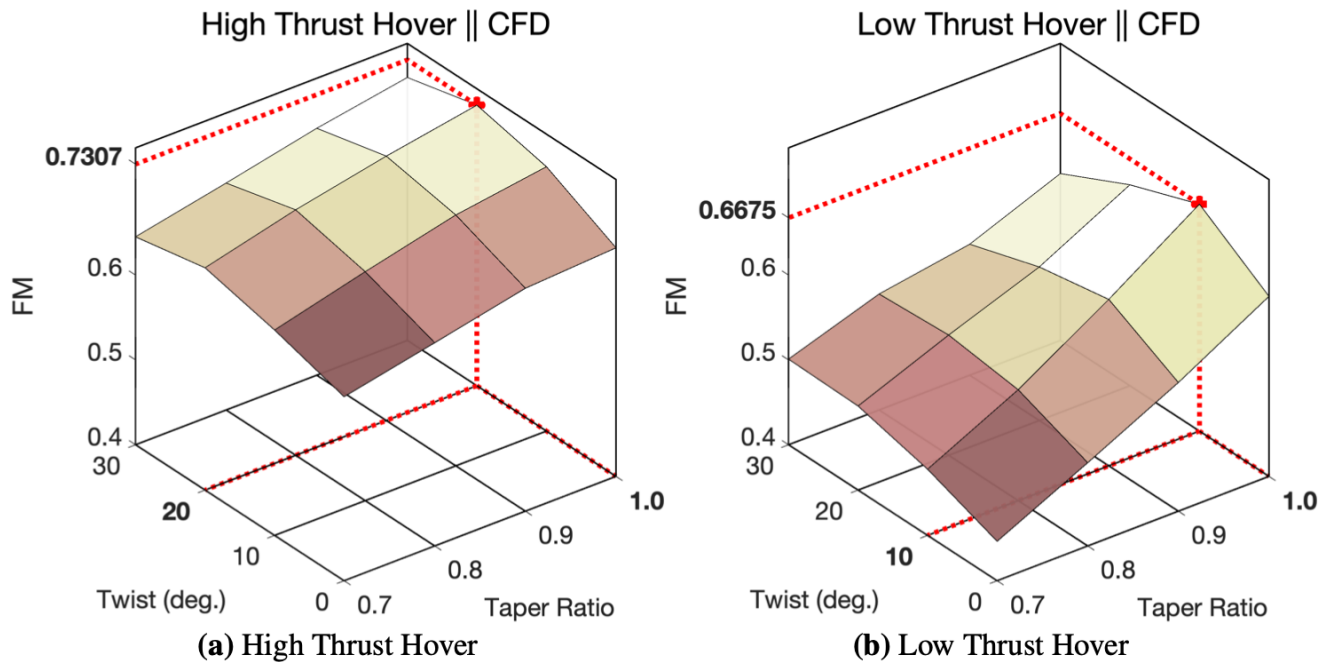


Figure 4. Surface plot of FM with respect to θ and λ for both high thrust hover (a) and low thrust hover (b) based on the 16 CFD runs for each case.

for percent energy retention per POD mode retention count can be found in Fig. 5 (b). Results of this analysis demonstrated
 310 that despite the increase in complexity of the spatial information in the domain, the POD algorithm still appears to be capable
 of efficiently capturing this information in a limited mode retention count.

Once a POD mode retention count of 8 was selected, POD modes were projected back to the domain to evaluate POD ROM
 reconstruction capability. In evaluating load reconstruction capabilities of surface pressure distribution for case **c4**, shown in
 Fig. 6 for both collective cases of hover, it can be seen that loads are being modeled with a high degree of fidelity in comparison
 315 to CFD. Pressure coefficient distributions at the $r/R = 0.95$ radial station are shown to be correctly accounted for with the
 reduced representation. The maximum percent error between CFD and ROM surface pressures for all 16 reconstructions for all
 radial stations was 1%. This deviation for both high and low thrust hovering cases was located at the stagnation location near the
 $r/R = 0.95$ radial station of the blade. Historically, modeling flow features with large gradients through modal decomposition
 techniques with minimum mode retention counts has proven challenging, particularly as these gradients move within the
 320 domain. For the case of the hovering rotor, the largest pressure gradients in the domain occur at the stagnation location. The
 spatial position of this location on the blade then varies as a function of θ , λ , and r/R . Yet, despite these challenges, the results
 of this study show that leading-edge gradients are captured with sufficient accuracy so that FM is still being modeled with
 a high degree of fidelity. The maximum percent error for reconstructed FM for both high and low thrust hover was 0.41%.
 Percent errors in FM reconstructions are shown in Table 3.

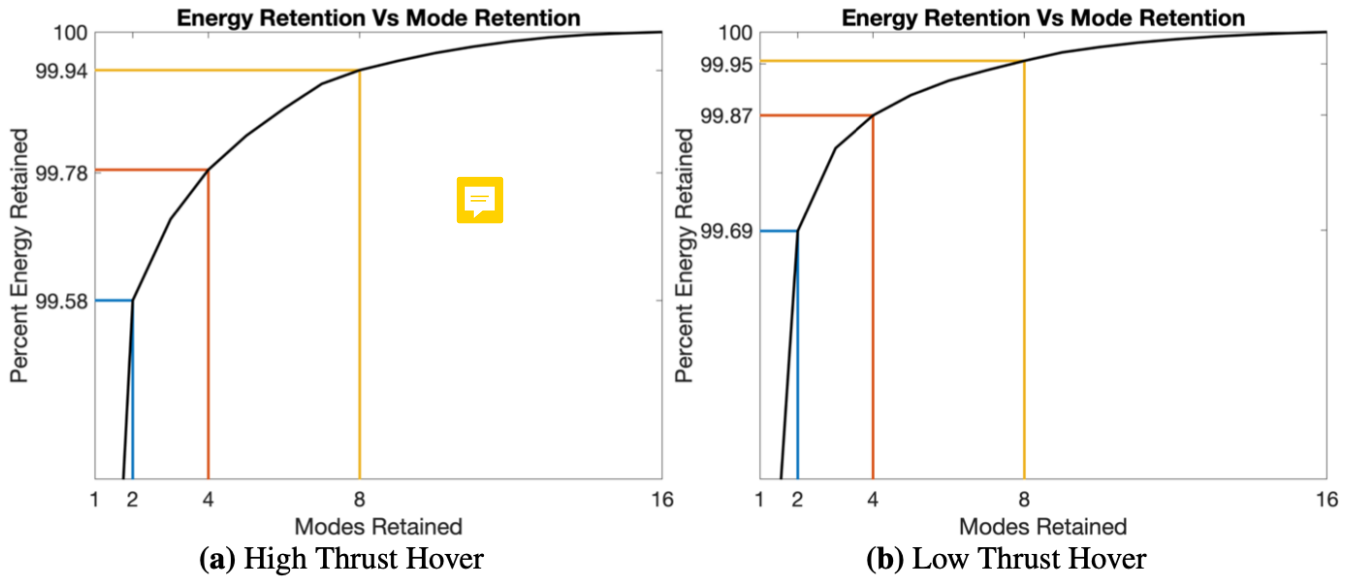


Figure 5. Percent energy retention per retained mode count for 2, 4, and 8 POD modes. Results are shown for both high thrust hover (a) and low thrust hover (b).

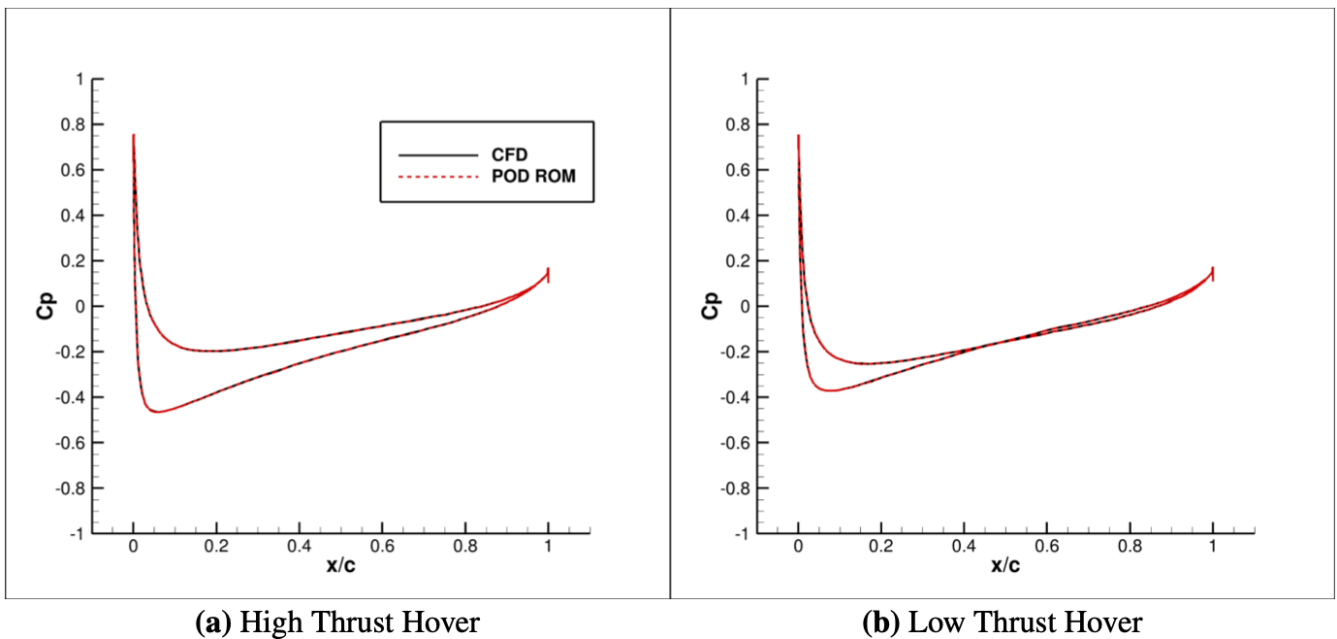


Figure 6. Comparison between POD ROM and CFD for slices of coefficient of pressure at $r/R = 0.95$. Comparison is shown for sample geometry **c4** in both high thrust hover (a) and low thrust hover (b).



Table 3. Maximum percent error between CFD and POD ROM computed FM for geometries **c1** to **c16**.

		Twist(deg) θ			
		0°	10°	20°	30°
Taper Ratio λ	1.0	0.20	0.36	0.19	0.04
	0.9	0.06	0.09	0.07	0.16
	0.8	0.01	0.10	0.12	0.41
	0.7	0.11	0.07	0.08	0.08

325 4.1.2 Hovering ROM Validation

After constructing the POD ROM and comparing reconstructs to CFD solutions, the study then moved to quantify POD ROM predictive capabilities for the geometries outlined in Table 2 for both high and low thrust demonstration cases. This validation was completed in two steps. First, distributed coefficients of pressure were compared between POD ROM prediction and CFD simulation after which these loads were integrated to identify FM . When comparing surface pressure distributions for both high and low thrust hover, shown in Fig. 7, it was found that with a minimum mode count the POD ROM was capable of providing high-fidelity full distributed load predictions for all three validation geometries. Surface pressure predicted error never exceeded 1.5% error compared to the CFD simulation in all validation comparisons.

330 These predicted surface pressures were then integrated to find FM . When comparing this FM to CFD for the high thrust hover cases it was found that for all three validation geometries percent error never exceeded 1%, thus providing strong evidence that a POD ROM can be efficiently deployed to model a rotor blade’s full distributed load with a high degree of fidelity. Summary of prediction capabilities for POD ROM is shown in Table 4.

Table 4. Summary of percent errors in coefficient of thrust, torque, and figure of merit predictions using POD ROM derived for low thrust hover.

Geometries	C_T	C_Q	FM
v1	0.47%	0.62%	0.09%
v2	0.03%	0.81%	0.77%
v3	0.80%	0.84%	0.37%

However, the same level of fidelity in integrated load comparison was not achieved once the rotor collective was decreased. While percent error for validation geometry **v1** was limited to 0.5%, the same level of fidelity was not achieved for validation geometries **v2** and **v3** as shown in Table 5. Surface pressure prediction errors once again never exceed a maximum of 1.5% for the low thrust hover. Yet, this error is shown to now occur over a sufficiently larger region of the blade thus resulting in

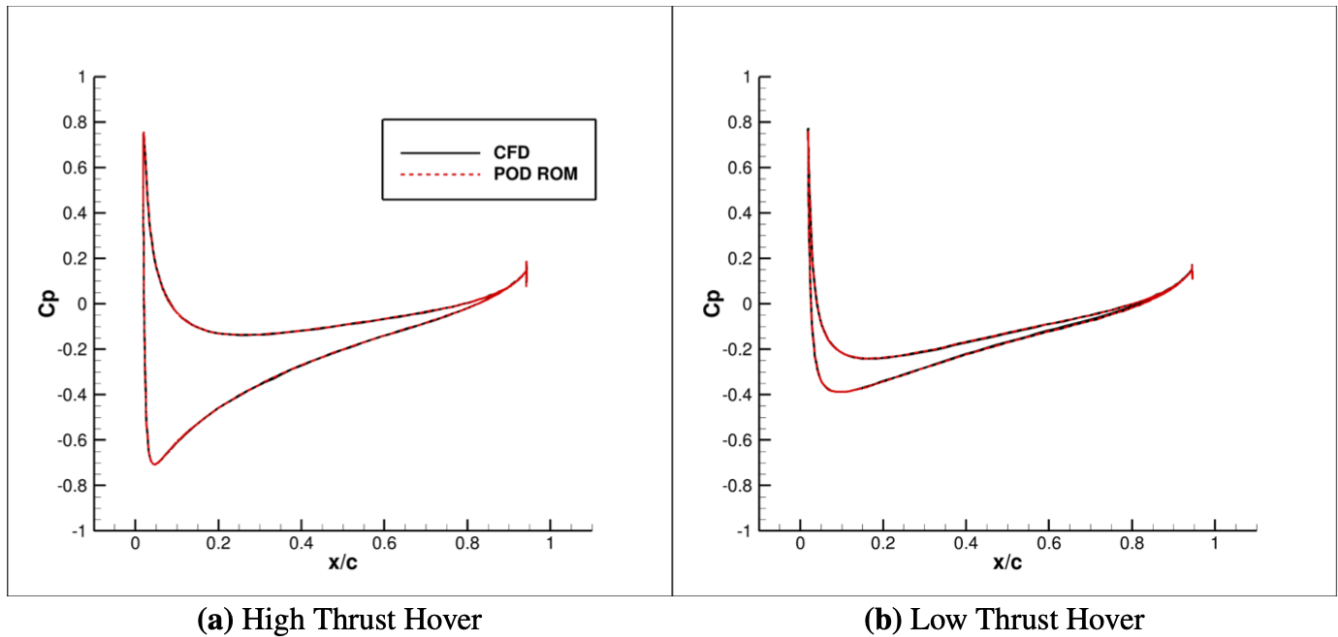


Figure 7. Comparison between POD ROM and CFD for slices of coefficient of pressure at $r/R = 0.95$. Comparison is shown for validation geometry **v3** in both high thrust hover (a) and low thrust hover (b).

a significant increase in integrated load error, raising FM prediction error from 0.77% and 0.37% for cases **v2** and **v3** of the high thrust hover to 4.26% and 4.25% for the low thrust hover. Results of the low thrust rotor case show that the capability of a POD ROM to make accurate load predictions is highly dependent on how well-sampled is the domain of interest.

While this conclusion may be intuitive, properly achieving a level of sufficient sampling is not. Even in this relatively simple
345 demonstration, it has been observed that by simply varying the rotor's collective there became a significant increase in design space complexity. While this increase in complexity was not limiting to POD ROM reconstruction capabilities, it was shown to have a significant deterioration in POD ROM prediction capabilities. Thus, as the design space complexity increased and domain sampling remained the same, there became an under-sampling of λ in the low thrust hover domain. These results highlight how often this task of achieving sufficient sampling of a domain may become an iterative task, requiring a further
350 refinement of the sampling of the domain. To construct a more accurate ROM in the case of low thrust hover, further sampling with new λ in this domain is required.

Yet, even with the limited sampling on the domain the POD ROM is still providing reasonably accurate predictions once accounting for the significant reduction in computational expense in evaluating each validation case. For both high and low thrust hover, surface pressures as computed by CFD required 12 hours of computing time across 440 cores. Meanwhile, the
355 POD ROM was capable of making comparable predictions of surface pressures in just a fraction of a second on a single core. In addition, prior CFD sampling of the low thrust hover domain indicated that local optimal FM was consistently located at $\lambda = 1.0$ and thus resulting in an optimization dependent on finding an optimal θ . For the case of low thrust hover, it was identified



Table 5. Summary of percent errors in coefficient of thrust, torque, and figure of merit predictions using POD ROM derived for low thrust hover.

Geometries	C_T	C_Q	FM
v1	0.23%	0.15%	0.49%
v2	0.80%	2.94%	4.26%
v3	1.65%	1.69%	4.25%

that the POD ROM was capable of providing high fidelity predictions for variations in θ . Given this prior knowledge of the domain and the significant reduction in computational expense, it became possible to directly apply this POD ROM to undergo a design optimization of the rotor blade to derive a local maximum of FM . Results showed that a optimal geometry of $\theta = 21.7^\circ$ and $\lambda = 1.0$ for high thrust hover and $\theta = 10^\circ$ and $\lambda = 1.0$ for low thrust hover could be found while taking 1 minute of compute time on a single core. A total of 20 iterations were required to obtain the optimal solution. These results show that by sampling a given design space a POD ROM can be efficiently derived such that a low cost and accurate model of the blade's surface pressures can be obtained and practically deployed to a relevant rotor design task.

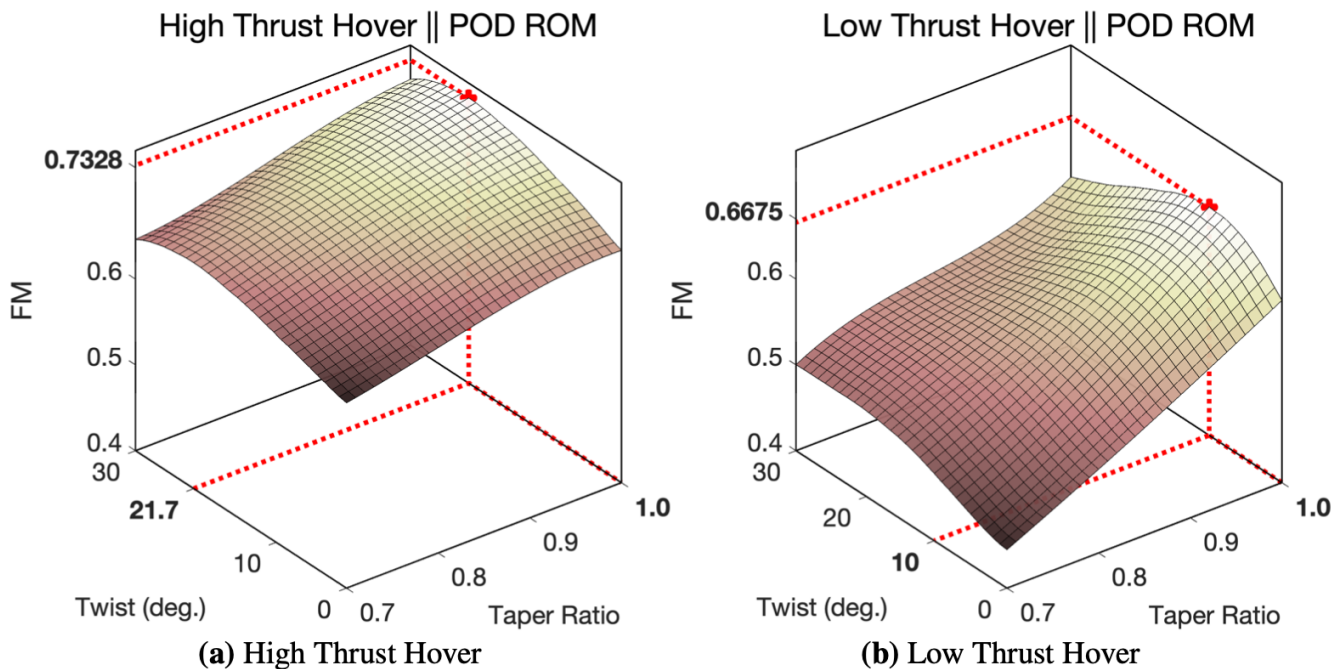


Figure 8. Surface plot of FM with respect to θ and λ as computed through POD ROM derived for high thrust hover (a) and low thrust hover (b).



365 In addition to providing an efficient means for identifying local optimal positions within a domain, the significant reduction to computational expense additionally provides the capability to efficiently obtain an increased understanding of the design space of interest. Given the high expense of CFD modeling and only a limited sampling of any domain of interest can be achieved. Yet, the results of this study have demonstrated how this limited sampling can be leveraged to obtain high accurate, low-cost models capable of providing an increased understanding of the domain of interest. When analyzing surface plots for FM as computed via CFD, only a limited representation of the domain can be achieved. However, by leveraging a validated POD ROM orders of magnitude more sampling points of the domain can be achieved, thus producing an increased resolution of the domain of interest. To demonstrate this capability, 900 additional samples of the domain were obtained via surface pressure predictions provided by the POD ROM and blade geometries generated through the study's grid generation algorithm. Results of this analysis are presented in Fig. 8. While this further analysis indicated that local optimal of both CFD and POD ROM representation of the low thrust hover domain results in the same local optimal FM , results for high thrust hover highlight how a POD ROM can be leveraged to help possibly identify previously unknown optimal locations within the design space.

4.2 Forward Flight

Up to this point in the study, the focus has been placed on hovering rotor blades. Given that these cases would produce a pressure distribution that was invariant to changes in azimuth, the study could limit the focus of POD ROM modeling capability to spatial information and thus limit the snapshot matrix to a set of 16 snapshots. However, for practical implementation, it is essential to demonstrate the applicability of ROM for both spatial and time varying domains. As such, in this section, a POD ROM based surrogate model will be used for the prediction of load distribution of a rotor in forward flight.

There are numerous challenges that may arise for extending the POD ROM to rotors in forward flight. The most prevalent of which is the increase in non-linear relationship between design variables and surface pressures. To construct contour plots shown in Fig. 9, C_T is computed locally at each radial station of the rotor at azimuth increments of 4.5° . As shown in Fig. 9, case **c4** ($\lambda = 1.0, \theta = 30^\circ$) and case **c5** ($\lambda = 0.9, \theta = 0^\circ$) have widely differing C_T distributions between azimuth of 0° - 60° and a spanwise position up to $r/R=0.50$. This variation is a result of flow separation occurring as the blade travels counter clockwise past zero azimuth position. From Fig. 9 it can be seen that through varying θ and λ , the degree to which flow will separate on the blade will vary greatly. This flow separation and reattachment provide a significant increase in data-set complexity which could potentially exacerbate the issue of POD ROM either not having enough sample points to make meaningful interpolations or not being capable of representing the system with low mode retention counts. The latter of these issues will be addressed in the next section.

Contributing to the difficulties of modeling the forward flight case are differing influences λ and θ have on rotor L/De . In Fig. 10 L/De as computed from integrated CFD modeled pressure loads are plotted versus λ and θ . Results demonstrate the significant parabolic influence θ has over blade load distributions. Rotor L/De is shown to exponentially decrease as θ deviates from 10° . This relationship is in contrast to the linear and relatively small influence λ has on L/De . For the hovering rotor cases, POD ROM was shown capable of modeling a multi-variable system with each variable holding a varying degree of influence over the system. Yet, the forward flight case provides a more extreme case of multi-variable modeling wherein there is clearly

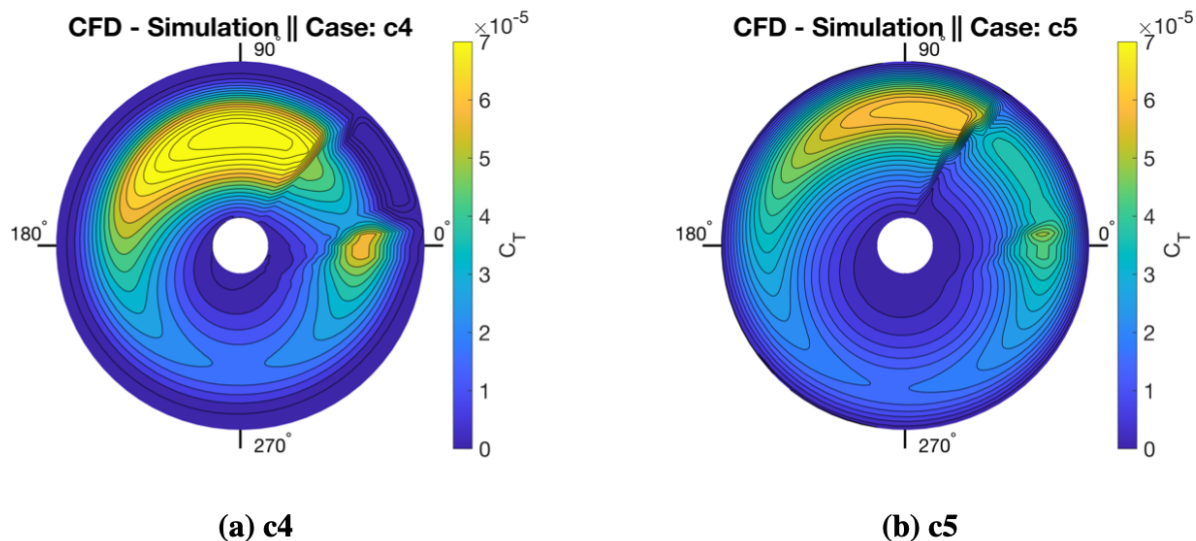


Figure 9. Contours of C_T as the blade rotates from an azimuth of 0° to 360° . Incoming flow is entering from the 180° direction while blade is rotating counter clockwise.

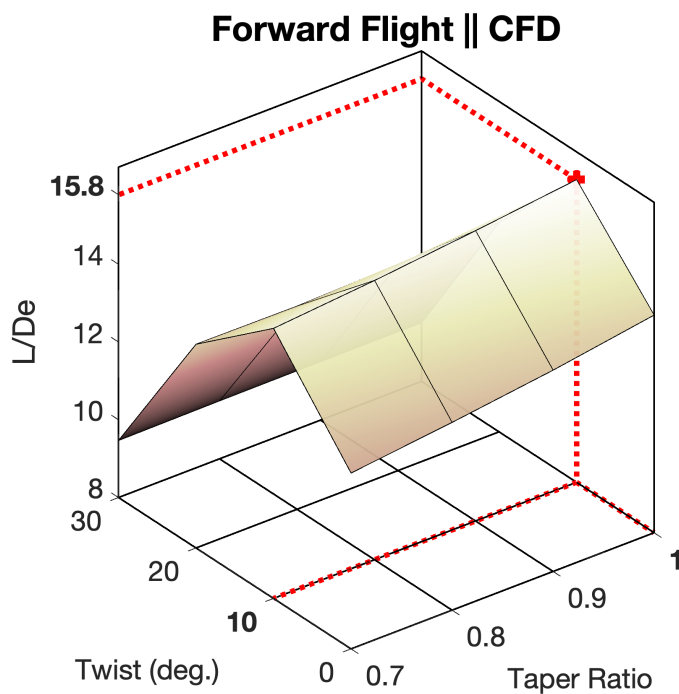


Figure 10. Surface plot of L/De with respect to θ and λ as computed through CFD.



a dominant term in the domain. Thus, the modeling challenge present in the forward flight case will include demonstrating that while POD ROM is truncating low energy information from the system, it does not truncate interdependencies between input parameters and blade surface pressure distributions.

4.2.1 ROM Reconstruction

After all 16 forward flight, CFD simulations were completed, a single snapshot matrix was formed. To form this snapshot matrix, solutions for rotor pressure distributions were written every 4.5 degrees such that sufficient resolution would be obtained to model both separation and reattachment flow at the correct azimuth angles. As a result, for each CFD simulation, 7 snapshots for rotor surface pressures were retained corresponding to a single snapshot matrix with 1184 snapshots. After completing this snapshot matrix, the POD algorithm was used and the percent energy retention per POD mode retention count was plotted and results are presented in Fig. 11. Given the significant increase in energy content in the system in comparison to the hovering rotor cases, energy retention was decreased to 90% so as to avoid retaining an excessive number of POD modes. It was identified that 16 POD modes were required to hit this energy retention criterion.

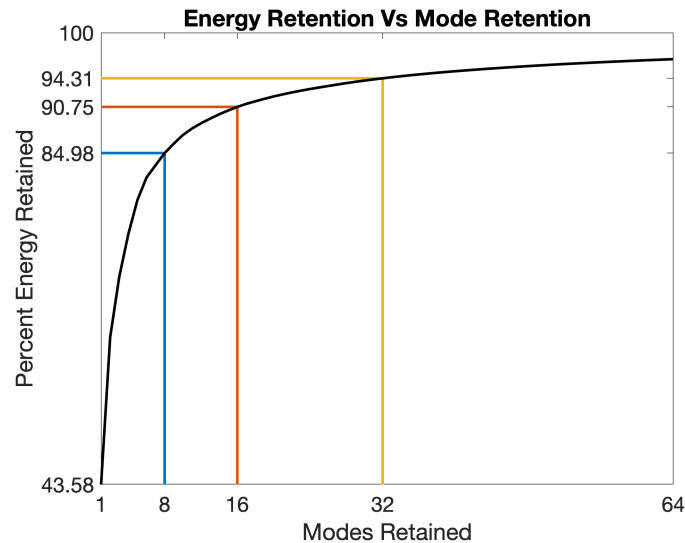


Figure 11. Percent energy retention per retained mode count for 8, 16, and 32 POD modes.

After undergoing the POD algorithm and identifying the number of retained POD modes, the study projected these modes back to the original snapshot matrix to identify how well the domain of interest is represented with the selected mode count. Reconstructions and reconstruction error can be found in Figures 12 and Figures 13. This observation provides two important conclusions. First, through the addition of flow separation and a varying azimuth angle, the energy content in the training data-set has been expanded. This expansion in energy content has led to an increase in the required mode retention count to obtain independent reconstructions.

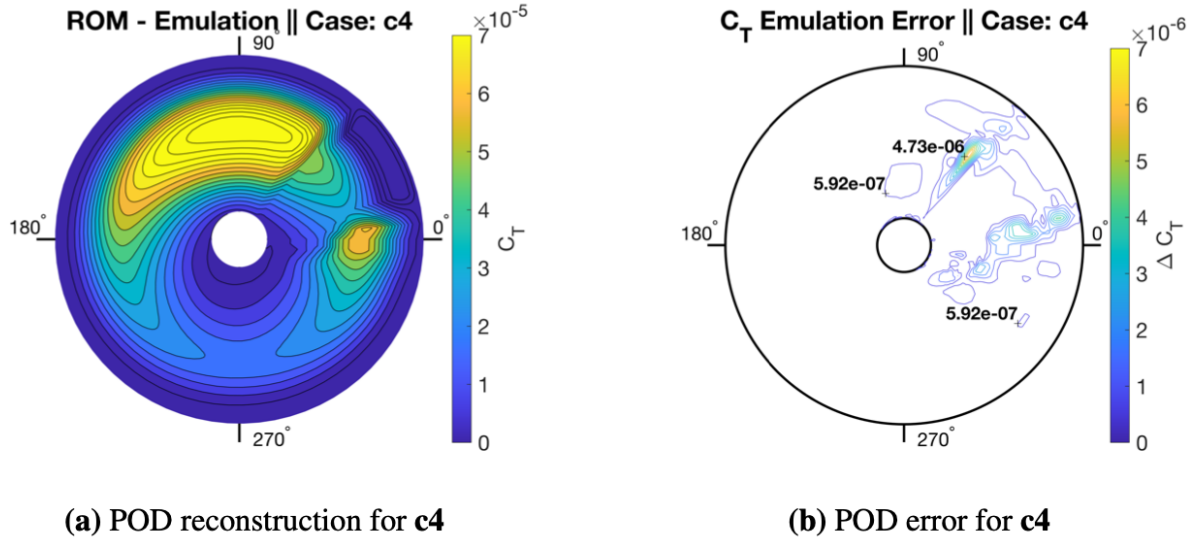


Figure 12. Contours of POD reconstruction for the CFD data of Fig 9 (a) and error for C_T as the blade rotates from an azimuth of 0° to 360° . Incoming flow is entering from the 180° direction while blade is rotating counter clockwise.

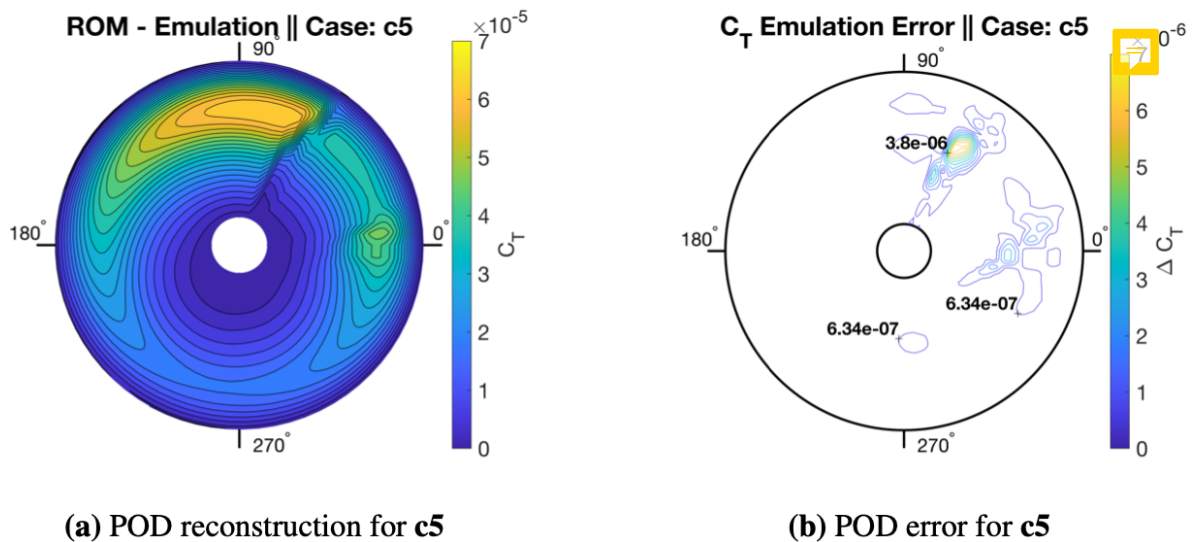


Figure 13. Contours of POD reconstruction for the CFD data of Fig 9 (b) and error for C_T as the blade rotates from an azimuth of 0° to 360° . Incoming flow is entering from the 180° direction while blade is rotating counter clockwise.

The second important observation is that despite the expansion in energy content, POD is shown to be capable of representing the full rotor disks of all 16 geometries with only 16 modes. For accurate reconstructions, modes retained were limited to modes with reasonably smooth variation with respect to θ and λ . These results highlight that the POD algorithm appears to



420 be exceptionally well suited for applications modeling periodic pressure distributions of rotors. The maximum percent error of C_T found for reconstructions of all 16 geometries was found to be below 0.1%. Not only were sectional C_T shown to be modeled accurately, but also integrated values for L/De . Maximum percent error for reconstructions of all 16 geometries was found to be 1.39%. Percent errors for all 16 geometries are outlined in Table 6. In the following section, the effect of increased distributed load complexity on POD ROM prediction capabilities will be demonstrated.

Table 6. Maximum percent error between CFD and POD ROM computed L/De for geometries **c1** to **c16**.

		Twist(deg) θ			
		0°	10°	20°	30°
Taper Ratio λ	1.0	0.0043	0.18	1.13	0.28
	0.9	0.10	1.39	0.46	0.11
	0.8	0.41	1.27	0.28	0.058
	0.7	0.73	1.13	0.23	0.24

425 4.2.2 ROM Validation

Further validation of POD ROM in forward flight predictions are produced for geometries **v1**, **v2**, and **v3** and compared to CFD simulation. Both prediction and error contours of sectional C_T for all three validation geometries are summarized in Fig. 14. Results show that for all three validation cases, the POD ROM is making highly accurate predictions for C_T across the rotor's complete cycle. For the vast majority of the motion of the blade, load distributions are being predicted almost exactly.

430 The distributed load prediction error is largely limited to the correct prediction of flow separation and reattachment azimuth angles positions. Results demonstrate that once the flow is either separated or attached, POD ROM is capable of producing high-fidelity distributed load predictions. In addition to comparing rotor disk C_T , rotor performance predictions via integrated L/De are compared between CFD simulation and POD ROM emulation. Results, shown in Table 9, demonstrate that the POD ROM is capable of providing highly accurate rotor performance predictions subject to both variations in twist and taper ratios


435 of the rotor. The maximum percent error never exceeds 0.1% compared to CFD simulation.

These observations underline the two critical takeaways from this study. First, if a modal decomposition algorithm is to be deployed for surface pressure modeling it must be capable of efficiently representing a complex domain. In this study, it has been shown that for a wide variety of operating conditions the POD algorithm has shown to perform exceptionally well at representing rotor surface pressures with minimum mode retention counts.


440 The second observation is that for the application of POD ROM to rotor surface pressure modeling, a sub-space must be sufficiently sampled such that the influence of design variables on load distributions is fully captured. It is important to note that prior knowledge of a system, particularly when applied to UAM aircraft, may be limited. As such, prior understanding of the



required sample size may not be held and an iterative approach must be taken to find the sufficient sampling size required for a POD ROM. When investigating the high thrust rotor, this study found that 16 samples were sufficient to provide near-exact
445 predictions for surface pressures. Yet, when considering the low thrust rotor it was identified that while efficient reconstructions could be made through POD, more sampling conditions were required for accurate interpolations. This was due to an increase in design space complexity with respect to λ .

For the case of a rotor in forward flight it was found that similar to high thrust rotors, the design space could be represented except ly well with the 16 sampling cases. Yet, a deeper analysis of POD modes demonstrates that the total number of CFD
450 sampling cases required to model the rotor's disk could be further reduced. In Fig. 16 a through c, variation of POD modes 1, 2, and 8 with respect to θ and λ are plotted. Results indicate that initial POD modes are linearly varying within the system while for mode counts 8 and up the mode relationship to design variables becomes significantly non-linear. These results highlight that the majority of the energy for the rotor in forward flight is varying linearly. To demonstrate the dominance of linearly determined variance in the system, a POD ROM was derived from retaining just four sampling points, cases **c1,c4,c13**, and
455 **c16**, thus producing only a linear mapping. In Fig. 15, C_T errors are presented for all 3 validation cases once only 4 sampling conditions are used. Results for sectional C_T integrated from POD ROM surface pressure predictions are comparable to those obtained when using all 16 CFD simulation sampling points. Results also demonstrate that an accurate representation of total integrated lift can be obtained from the derived model with percent errors for rotor lift predictions never exceeded 1%, presented in Table 7. Yet, while rotor lift predictions were shown to retain a high degree of fidelity, there was a significant deviation in
460 rotor power predictions. Thus, the results of this analysis indicated that rotor lift performance is dominated by linearly varying high energy POD modes while rotor drag performance is dominated by the non-linear low energy POD modes.

To improve power performance predictions of the POD ROM, the number of sampling points can be increased such that an accurate representation of the non-linear variation of the low-energy POD modes can be obtained. It should be noted that this non-linear variation is limited to variation in the θ space. As such to achieve this increased representation of low-energy
465 POD mode variation a combination of four θ and two λ sampling points were retained such that a POD ROM was derived from cases **c1, c2, c3, c4,c13, c14, c15**, and **c16**. Results for rotor performance predictions with this POD ROM are presented in Table 8 and demonstrate that despite halving the number of sampling points from 16 to 8 similar levels of fidelity for rotor performance predictions can still be achieved.

Just as in the hovering cases, there was a significant reduction in computational expense obtained when using the reduced
470 model. The POD ROM evaluation of rotor surface pressures across the entire periodic motion took a fraction of a second on a single core. Meanwhile, the CFD simulation required 20 hours on 440 cores. Once applied to design optimization of the rotor such that local optimal L/De was obtained, an optimal solution was found within 10 minutes of computing time on a single core. Results of this optimization, along with surface mappings constructed from obtaining 900 additional rotor performance predictions of the domain, are plotted in Fig. 16 for both POD ROM derived from 4, 8, and 16 CFD sampling points. All three
475 optimization results hint at a significant capability of POD ROM to efficiently extract mea ful information from a domain of interest with limited sampling such that a greater understanding of the design space can be obtained. In Fig. 16 (d), it is shown that despite only ever sampling the corners of the domain and thus deriving linear relationships the non-linear influence θ holds



over rotor performance can still be captured. While this influence is exaggerated in magnitude, resulting from inconsistencies in modeling power requirements, the overall trend of this influence is preserved such that a previously unknown local optimal solution in the area of $\theta = 12.4^\circ$ and $\lambda = 1$ can be obtained. By doubling sampling size from 4 to 8, shown in Fig. 16 (e), results show that not only can a relevant local optimal design point be identified but a higher level of fidelity can be achieved for performance predictions. Through further increasing sampling of the domain, shown in Fig. 16 (f), it is hinted that there perhaps exist additional local optimal solutions within the design space as θ goes from 6° to 12° and λ goes from 0.7 to 1. While POD ROM derived from all 16 sampling points identified a local optimal solution of $L/De = 16.1$ at $\theta = 6.21^\circ$ and $\lambda =$
480
485 0.96, the second optimal solution found using this model was $L/De = 16.0$ at $\theta = 11.5^\circ$ and $\lambda = 1$. The second optimal solution found using POD ROM derived from 16 sampling points was less than a single degree off from the optimal solution obtained using only 4 sampling points.



Table 7. Summary of percent errors in lift (L), power (P), and L/De predictions using POD ROM from 4 training points (cases **c1,c4,c13**, and **c16**).

Geometries	L	P	L/De
v1	0.61%	62.4%	164%
v2	0.21%	0.45%	0.24%
v3	0.23%	64%	178%

Table 8. Summary of percent errors in lift (L), power (P), and L/De predictions using POD ROM from 8 training points (cases **c1, c2, c3, c4,c13, c14, c15**, and **c16**).

Geometries	L	P	L/De
v1	0.30%	0.42%	0.13%
v2	0.09%	0.13%	0.04%
v3	0.17%	3.02%	3.26%

Table 9. Summary of percent errors in lift (L), power (P), and L/De predictions using POD ROM from 16 training points.

Geometries	L	P	L/De
v1	0.13%	0.23%	0.10%
v2	0.065%	0.30%	0.24%
v3	0.05%	0.47%	0.41%

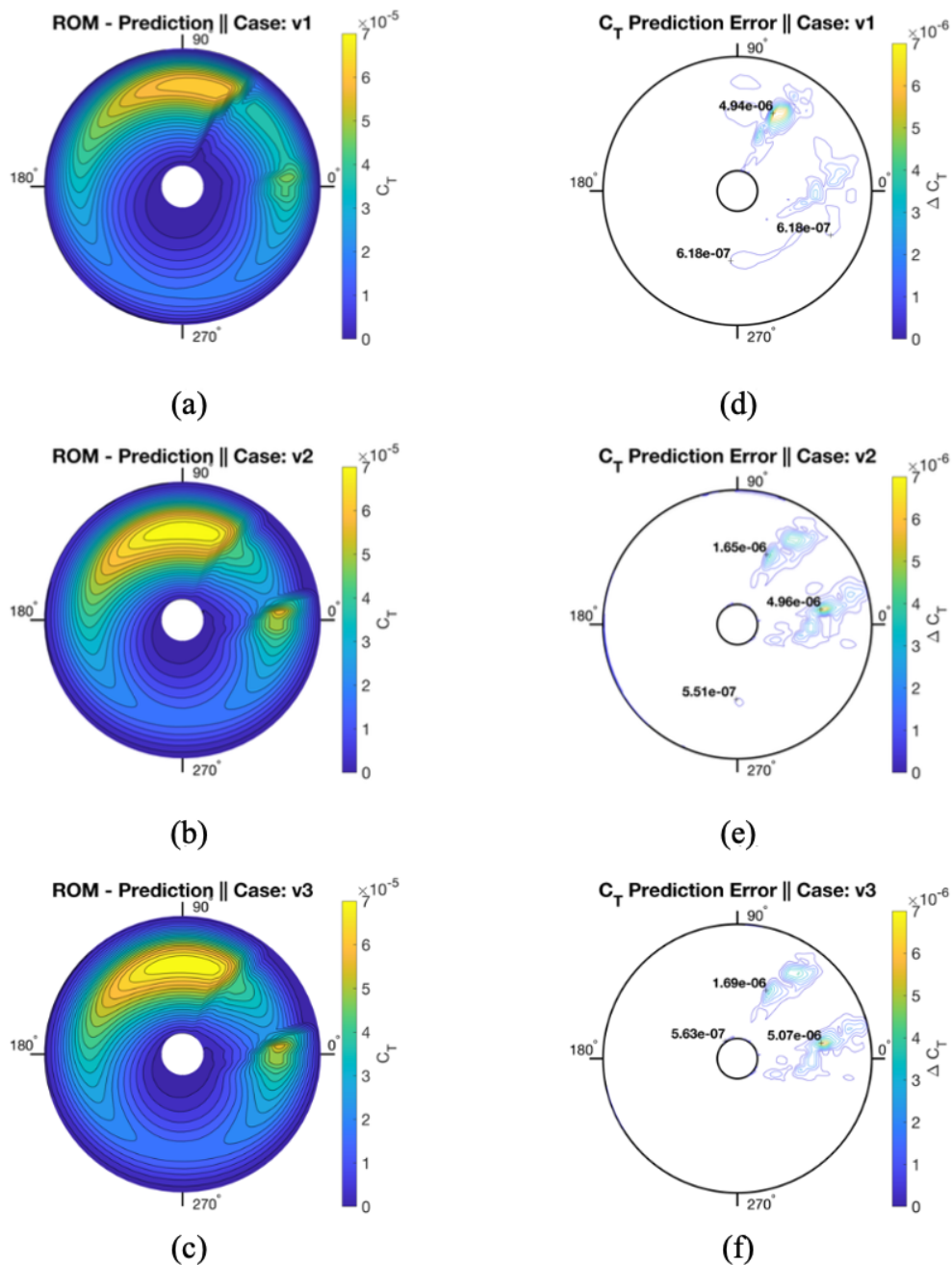


Figure 14. Contours of POD ROM prediction and error compared to CFD using 16 sample cases for rotor's coefficient of thrust, C_T , as the blade rotates from an azimuth of 0° to 360° . Incoming flow is entering from the 180° direction while blade is rotating counter clockwise.

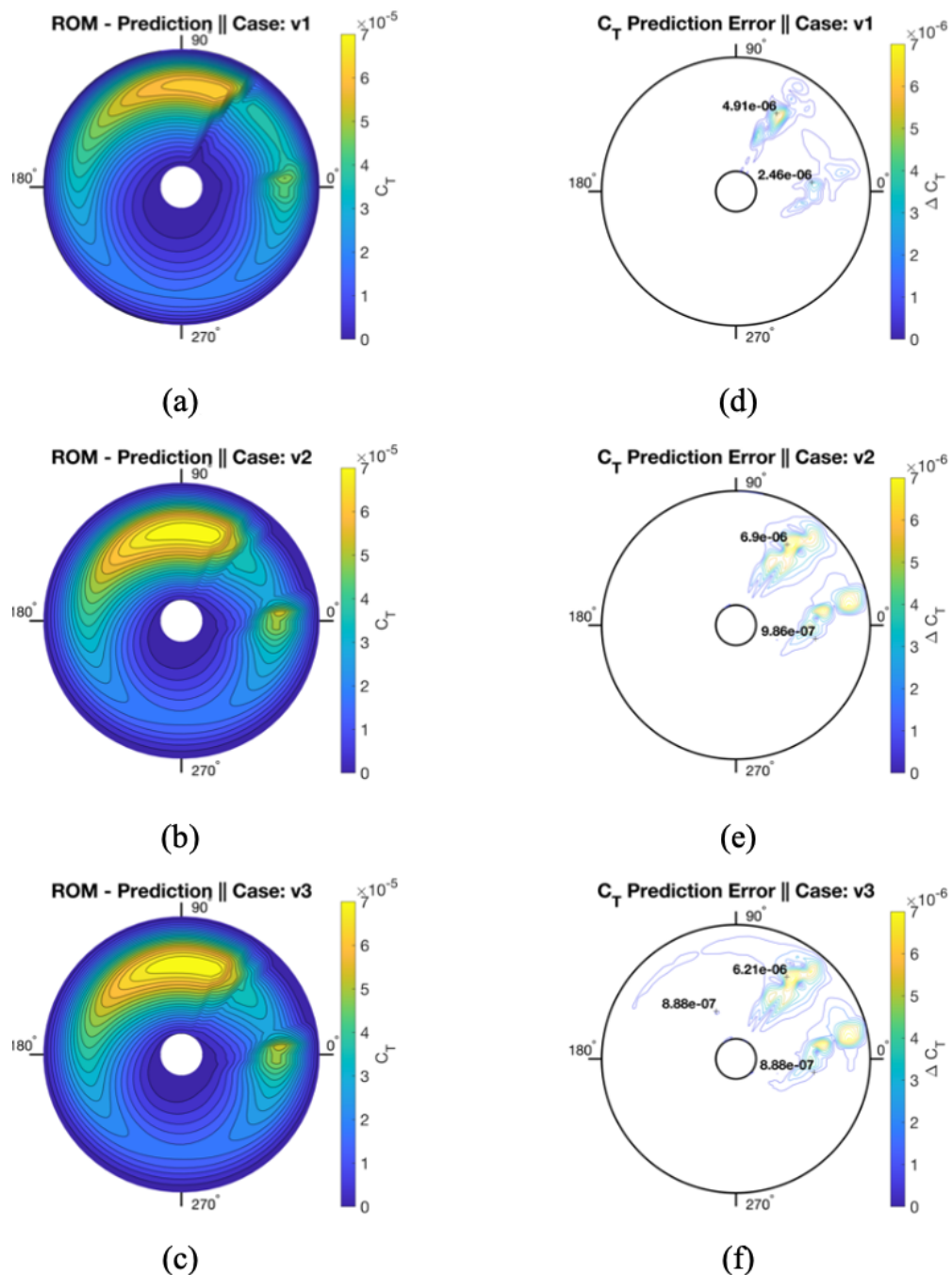


Figure 15. Contours of POD ROM prediction and error compared to CFD using 4 sample cases for rotor’s coefficient of thrust, C_T , as the blade rotates from an azimuth of 0° to 360°. Incoming flow is entering from the 180° direction while blade is rotating counter clockwise.

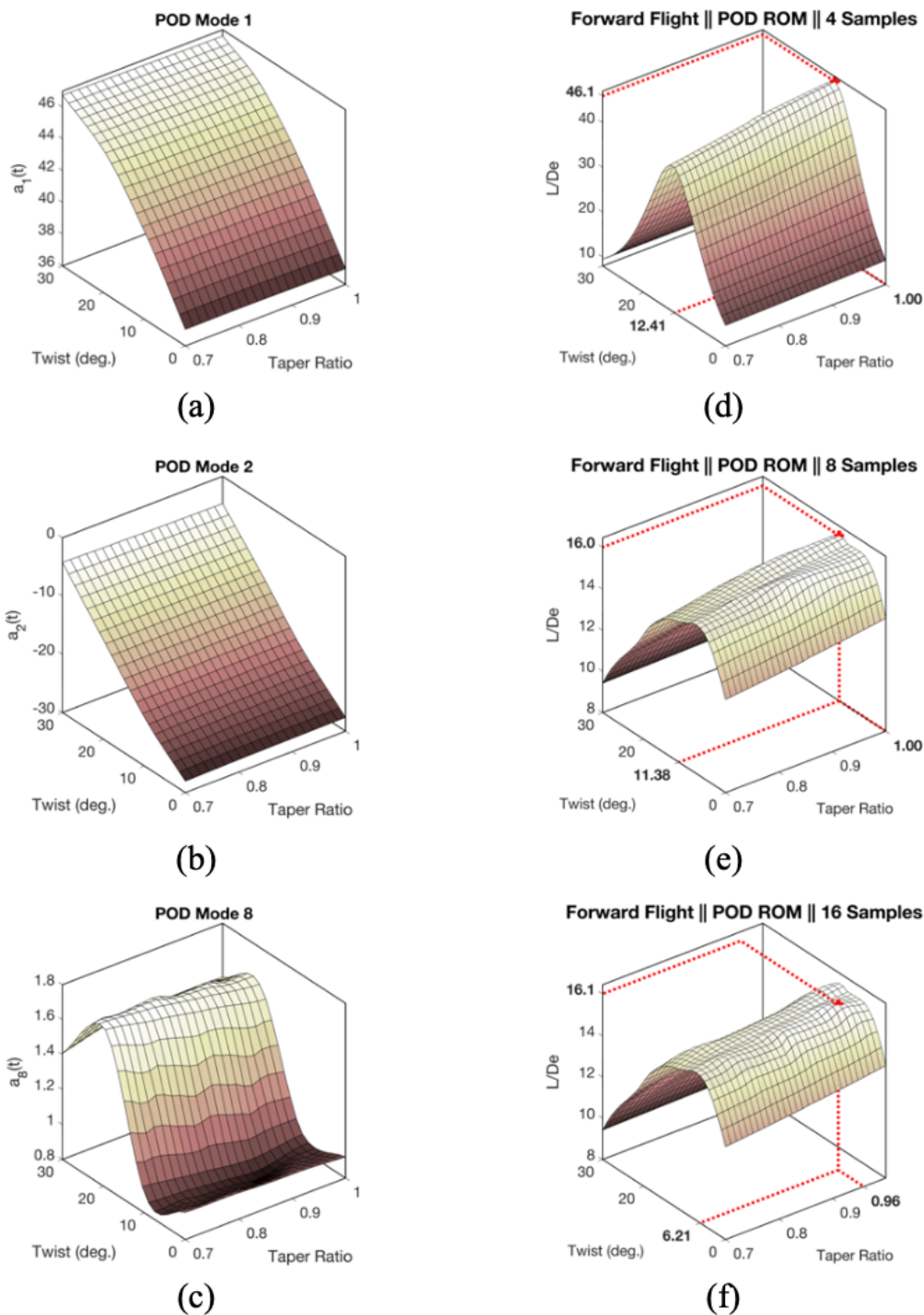


Figure 16. Left Column: Surface plots showing both linear and spline representation of POD modes 1, 2, and 8. Right Column: Surface plot of L/De with respect to θ and λ as computed through POD ROM derived from 4 samplings points (d), 8 sampling points (e), and 16 sampling points (f).



5 Conclusions

In this study, a POD ROM was applied to three demonstration cases for distributed pressure load predictions of a single blade model rotor. Namely, these cases were high thrust hovering rotor, low thrust hovering rotor, and rotor in forward flight. For each of these cases, blade twist and taper ratio were varied such that 16 blade geometries were used. All three POD-based surrogate ROMs were shown to produce highly accurate predictions for surface pressure distributions. For both high thrust rotor and forward flight ROMs, the maximum integrated load coefficient prediction error was below 1%. The error was increased for low thrust rotor ROM but still limited to below 4.3%. When POD ROM was implemented, the computational expense was significantly decreased. For hovering rotor, the expense was reduced from 12 hours on 440 cores for CFD simulation to just a fraction of a second on a single core for ROM predictions. For forward flight rotor, the expense was reduced from 20 hours on 440 cores to less than a second on a single core when POD ROM was implemented. The expense was reduced to the extent that a design optimization became feasible for both hovering and forward flight demonstration cases. Results demonstrated how a POD ROM could be efficiently derived and deployed to model a complex design space to a high degree of fidelity. Additionally, it was demonstrated how this surrogate model could be both leveraged to quickly find optimal design points within the space and used to gain an enhanced understanding of the domain of interest.

While the present work provides strong evidence for the feasible application of POD ROMs to wind turbines and rotorcraft, there are still several future steps remaining for understanding POD ROM difficulties in rotor modeling. POD ROM modeling of multiblade rotors with realistic geometries and control surface coupling could be attempted. Future steps should also be taken to include wind farms operating with multiple rotor configurations. Additionally, CFD simulations should be completed using more complex operating conditions, such as turbulent inflows. By including these two modeling choices a more broad range of length scales will be introduced into the training data-set thus testing POD-based surrogate ROMs capability for efficiently extracting meaningful information in increasingly complex domains.

Code availability. Codes are available upon request.

Author contributions. Nicholas Peters ran all CFD simulations and generated all surrogate models presented for this study. Dr. John Ekaterinaris provided valuable insight during the generation of surrogate models while Christopher Silva assisted in devising relevant demonstration cases of surrogate modeling applied to rotors.

Competing interests. The authors declare that they have no conflict of interest.



515 *Acknowledgements.* The authors would like to thank Andrew Wissink and Ethan Romander for their insight as to best practices when using the OVERFLOW and CREATE-AV Helios Codes. The authors would additionally like to thank Haley Cummings, Ethan Romander, and William Warmbrodt of the NASA Ames Aeromechanics Branch for their invaluable feedback on this paper.



References

- Abhishek, A., Ananthan, S., Baeder, J., and Chopra, I.: Prediction and Fundamental Understanding of Stall Loads in UH-60A Pull-Up Maneuver, *Journal of the American Helicopter Society*, 56, 1–14, <https://doi.org/10.4050/JAHS.56.042005>, 2011.
- 520 Abras, Jennifer and Hariharan, Nathan S: Machine Learning Based Physics Inference from High-Fidelity Solutions: Vortex Classification and Localization, in: *AIAA Scitech 2022 Forum*, p. 310, San Diego, CA, <https://doi.org/10.2514/6.2022-0310>, 2022.
- Anusonti-Inthra, P.: Full Vehicle Simulations for a Coaxial Rotorcraft using High-Fidelity CFD/CSD Coupling, in: *2018 AIAA Aerospace Sciences Meeting*, p. 0777, Kissimmee, FL, <https://doi.org/10.2514/6.2018-0777>, 2018.
- Benek, J., Steger, J., Dougherty, F., and Buning, P.: *Chimera. A Grid-Embedding Technique*, 1986.
- 525 Brunton, S. L. and Kutz, J. N.: *Data-Driven Science and Engineering: Machine Learning, Dynamical Systems, and Control*, Cambridge University Press, <https://doi.org/10.1017/9781108380690>, 2019.
- Buning, P., Chiu, I., Obayashi, S., Rizk, Y., and Steger, J.: Numerical Simulation of the Integrated Space Shuttle Vehicle in Ascent, in: *15th Atmospheric Flight Mechanics Conference*, p. 4359, Minneapolis, MN, <https://doi.org/10.2514/6.1988-4359>, 1988.
- Chan, W. M., C. I. T. and Buning, P. G.: *User's Manual for the HYPGEN Hyperbolic Grid Generator and the HGUI Graphical User Interface*, 530 NASA TM-108791, 1993.
- Chan, W. M.: *Advances in Software Tools for Pre-Processing and Post-Processing of Overset Grid Computations*, in: *Proceedings of the 9th International Conference on Numerical Grid Generation in Computational Field Simulations*, San Jose, 2005.
- Chang, Y.-H., Zhang, L., Wang, X., Yeh, S.-T., Mak, S., Sung, C.-L., Jeff Wu, C., and Yang, V.: Kernel-Smoothed Proper Orthogonal Decomposition–Based Emulation for Spatiotemporally Evolving Flow Dynamics Prediction, *AIAA Journal*, 57, 5269–5280, 535 <https://doi.org/10.2514/1.J057803>, 2019.
- Chau, R.: *Process and Packaging Innovations for Moore's Law Continuation and Beyond*, in: *2019 IEEE International Electron Devices Meeting (IEDM)*, pp. 1–1, IEEE, San Francisco, CA, <https://doi.org/10.1109/IEDM19573.2019.8993462>, 2019.
- Chen, X., Liu, L., Long, T., and Yue, Z.: A reduced order aerothermodynamic modeling framework for hypersonic vehicles based on surrogate and POD, *Chinese Journal of Aeronautics*, 28, 1328–1342, <https://doi.org/10.1016/j.cja.2015.06.024>, 2015.
- 540 Cinquegrana, D. and Vitagliano, P. L.: A Reduced Order Model for Boundary Layer Ingestion Map Prediction at Fan Inlet of Rear-Mounted Engine Nacelle, in: *AIAA Scitech 2021 Forum*, p. 0993, <https://doi.org/10.2514/6.2021-0993>, 2021.
- Cizmas, P. G. and Palacios, A.: Proper Orthogonal Decomposition of Turbine Rotor-Stator Interaction, *Journal of Propulsion and Power*, 19, 268–281, <https://doi.org/10.2514/2.6108>, 2003.
- Colella, M., Saltari, F., Pizzoli, M., and Mastroddi, F.: Sloshing reduced-order models for aeroelastic analyses of innovative aircraft configurations, *Aerospace Science and Technology*, 118, <https://doi.org/10.1016/j.ast.2021.107075>, 2021.
- 545 Conley, S. and Shirazi, D.: Comparing Simulation Results from CHARM and RotCFD to the Multirotor Test Bed Experimental Data, in: *AIAA Aviation 2021 Forum*, p. 2540, VIRTUAL EVENT, <https://doi.org/10.2514/6.2021-2540>, 2021.
- Crozon, C., Steijl, R., and Barakos, G.: Coupled Flight Dynamics and CFD-Demonstration for Helicopters in Shipborne Environment, *Aeronautical Journal*, 122, 42–82, <https://doi.org/10.1017/aer.2017.112>, 2018.
- 550 DNV, G.: *Bladed User Manual: Version 4.9*, Gerrad Hassan & Partners Ltd.: Bristol, UK, 2018.
- Dreyer, E. R., Grier, B. J., McNamara, J. J., and Orr, B. C.: Rapid Steady-State Hypersonic Aerothermodynamic Loads Prediction Using Reduced Fidelity Models, vol. 58, pp. 663–676, <https://doi.org/10.2514/1.C035969>, 2021.



- Fitzgibbon, T., Woodgate, M., and Barakos, G.: Assessment of Current Rotor Design Comparison Practices based on High-Fidelity CFD Methods, *Aeronautical Journal*, 124, 731–766, <https://doi.org/10.1017/aer.2019.162>, 2020.
- 555 Ho, J. C., Jayaraman, B., and Yeo, H.: Coupled Computational Fluid Dynamics and Comprehensive Analysis Calculations of a Gimballed Tiltrotor, *AIAA Journal*, 57, 4433–4446, <https://doi.org/10.2514/1.J057394>, 2019.
- Holmes, P., Lumley, J. L., and Berkooz, G.: *Turbulence, Coherent Structures, Dynamical Systems and Symmetry*, Cambridge Monographs on Mechanics, Cambridge University Press, <https://doi.org/10.1017/CBO9780511622700>, 1996.
- Jin, Y., Lu, K., Hou, L., and Chen, Y.: An adaptive proper orthogonal decomposition method for model order reduction of multi-disc rotor system, *Journal of Sound and Vibration*, 411, 210–231, <https://doi.org/10.1016/j.jsv.2017.09.001>, 2017.
- 560 Johnson, W.: *CAMRAD II, Comprehensive Analytical Model of Rotorcraft Aerodynamics and Dynamics*, Johnson Aeronautics, Palo Alto, California, 1999, 1992.
- Johnson, W.: *NDARC-NASA Design and Analysis of Rotorcraft*, Tech. rep., 2015.
- Jonkman, J. M. and Buhl Jr, M. L.: *Fast user’s guide*-updated august 2005, report NREL/TP-500-38230, National Renewable Energy Lab.(NREL), Golden, CO (United States), <https://doi.org/10.2172/15020796>, 2005.
- 565 Keckskemety, K. M. and McNamara, J. J.: Influence of wake dynamics on the performance and aeroelasticity of wind turbines, *Renewable Energy*, 88, 333–345, <https://doi.org/10.1016/j.renene.2015.11.031>, 2016.
- Lakshminarayan, V. K., Sitaraman, J., and Wissink, A. M.: Application of Strand Grid Framework to Complex Rotorcraft Simulations, *Journal of the American Helicopter Society*, 62, 1–16, <https://doi.org/10.4050/JAHS.62.012008>, 2017.
- 570 Larsen, T. J. and Hansen, A. M.: *How 2 HAWC2, the user’s manual*, Risø National Laboratory, 2007.
- Liew, J., Urbán, A. M., and Andersen, S. J.: Analytical model for the power–yaw sensitivity of wind turbines operating in full wake, *Wind Energy Science*, 5, 427–437, <https://doi.org/10.5194/wes-5-427-2020>, 2020.
- Liu, H., Gao, X., Chen, Z., and Yang, F.: Efficient reduced-order aerodynamic modeling in low-Reynolds-number incompressible flows, *Aerospace Science and Technology*, 119, <https://doi.org/https://doi.org/10.1016/j.ast.2021.107199>, 2021.
- 575 Liu, Y., Lu, Y., Wang, Y., Sun, D., Deng, L., Wang, F., and Lei, Y.: A CNN-based shock detection method in flow visualization, *Computers & Fluids*, 184, 1–9, <https://doi.org/10.1016/j.compfluid.2019.03.022>, 2019.
- Ma, X., Karamanos, G., and Karniadakis, G.: Dynamics and low-dimensionality of a turbulent near wake, *Journal of Fluid Mechanics*, 410, 29–65, <https://doi.org/10.1017/S0022112099007934>, 2000.
- Morelli, M., Bellosta, T., and Guardone, A.: Development and preliminary assessment of the open-source CFD toolkit SU2 for rotorcraft flows, *Journal of Computational and Applied Mathematics*, 389, 113 340, <https://doi.org/10.1016/j.cam.2020.113340>, 2021.
- 580 Neerarambam, S., Bowles, P. O., Min, B.-Y., Lamb, D., Dunn, A. F., Frydman, J., Harrington, G., Lian, C., Kazlauskas, M., Wake, B. E., et al.: An Overview of the Exhaust Gas Reingestion Challenges on the CH 53K King Stallion, in: *AIAA Scitech 2021 Forum*, p. 0028, <https://doi.org/10.2514/6.2021-0028>, 2021.
- Nuernberg, M. and Tao, L.: Three dimensional tidal turbine array simulations using OpenFOAM with dynamic mesh, *Ocean Engineering*, 147, 629–646, <https://doi.org/10.1016/j.oceaneng.2017.10.053>, 2018.
- 585 Peters, N., Ekaterinaris, J. A., and Wissink, A. M.: A Mode Based Reduced Order Model for Supersonic Store Separation, in: *AIAA Aviation 2021 Forum, VIRTUAL EVENT*, <https://doi.org/10.2514/6.2021-2548>, 2021.
- Peters, N., Ekaterinaris, J., and Wissink, A.: A Mode Based Reduced Order Model for Rotorcraft Separation, in: *AIAA Scitech 2022 Forum*, San Diego, CA, <https://doi.org/10.2514/6.2022-0312>, 2022a.



- 590 Peters, N., Wissink, A., and Ekaterinaris, J.: Machine Learning Approaches and Surrogate Modeling of Store Separation, *Computers & Fluids*, 2022b.
- Peters, N., Wissink, A., and Ekaterinaris, J.: On the Construction of a Mode Based Reduced Order Model for a Moving Store, *Aerospace Science and Technology*, <https://doi.org/https://doi.org/10.1016/j.ast.2022.107484>, 2022c.
- Quackenbush, T., Wachspress, D., Boschitsch, A., and Curbishley, T.: A Comprehensive Hierarchical Aeromechanics Rotorcraft Model (CHARM) for General Rotor/Surface Interaction, CDI Report, pp. 99–03, 1999.
- 595 Raissi, M., Perdikaris, P., and Karniadakis, G.: Physics-informed neural networks: A deep learning framework for solving forward and inverse problems involving nonlinear partial differential equations, *Journal of Computational Physics*, 378, 686–707, <https://doi.org/https://doi.org/10.1016/j.jcp.2018.10.045>, 2019.
- Ramasamy, M., Johnson, B., and Leishman, J.: Turbulent Tip Vortex Measurements Using Dual-Plane Stereoscopic Particle Image Velocimetry, *AIAA Journal*, 478, 1826–1840, <https://doi.org/10.2514/1.39202>, 2009.
- 600 Rogers, S., Cao, H., and Su, T.: Grid Generation for Complex High-Lift Configurations, in: 29th AIAA, Fluid Dynamics Conference, p. 3011, Albuquerque, NM, <https://doi.org/10.2514/6.1998-3011>, 1998.
- Saberi, H., Khoshlahjeh, M., Ormiston, R. A., and Rutkowski, M. J.: Overview of RCAS and Application to Advanced Rotorcraft Problems, in: American Helicopter Society 4th Decennial Specialists' Conference on Aeromechanics, San Francisco, CA, 2004.
- 605 Sankaran, V., Sitaraman, J., Wissink, A., Datta, A., Jayaraman, B., Potsdam, M., Mavriplis, D., Yang, Z., O'Brien, D., Saberi, H., et al.: Application of the Helios Computational Platform to Rotorcraft Flow Fields, AIAA paper, 1230, 2010, <https://doi.org/10.2514/6.2010-1230>, 2010.
- Schmid, P. J.: Dynamic mode decomposition of numerical and experimental data, *Journal of Fluid Mechanics*, 656, 5–28, <https://doi.org/10.1017/S0022112010001217>, 2010.
- 610 Sengers, B. A. M., Zech, M., Jacobs, P., Steinfeld, G., and Kühn, M.: A physically interpretable data-driven surrogate model for wake steering, *Wind Energy Science*, 7, 1455–1470, <https://doi.org/10.5194/wes-7-1455-2022>, 2022.
- Sieber, M., Paschereit, C. O., and Oberleithner, K.: Spectral Proper Orthogonal Decomposition, *Journal of Fluid Mechanics*, 792, 798–828, <https://doi.org/10.1017/jfm.2016.103>, 2016.
- Sirovich, L.: *Quarterly of Applied Mathematics*, XLV, 3, 1987.
- 615 Smagorinsky, J.: General Circulation Experiments with the Primitive Equations: I. The Basic Experiment, *Monthly Weather Review*, 91, 99–164, [https://doi.org/10.1175/1520-0493\(1963\)091<0099:GCEWTP>2.3.CO;2](https://doi.org/10.1175/1520-0493(1963)091<0099:GCEWTP>2.3.CO;2), 1963.
- Sood, I., Simon, E., Vitsas, A., Blockmans, B., Larsen, G. C., and Meyers, J.: Comparison of Large Eddy Simulations against measurements from the Lillgrund offshore wind farm, *Wind Energy Science Discussions*, pp. 1–31, <https://doi.org/10.5194/wes-2021-153>, 2022.
- Spalart, P. and Allmaras, S.: A One-Equation Turbulence Model for Aerodynamic Flows, in: 30th Aerospace Sciences Meeting and Exhibit, p. 439, Reno, NV, <https://doi.org/10.2514/6.1992-439>, 1992.
- 620 Spalart, P. R.: Comments on the Feasibility of LES for Wings, and on a Hybrid RANS/LES Approach, in: Proceedings of first AFOSR international conference on DNS/LES, Greyden Press, <https://cir.nii.ac.jp/crid/1571698599231647232>, 1997.
- Walatka, P. P.: *PLOT3D User's Manual*, vol. 101067, NASA, 1990.
- Wang, H. and Zhai, Z. J.: Advances in building simulation and computational techniques: A review between 1987 and 2014, *Energy and Buildings*, 128, 319–335, <https://doi.org/10.1016/j.enbuild.2016.06.080>, 2016.
- 625



- Wissink, A. M., Sitaraman, J., Jayaraman, B., Roget, B., Lakshminarayan, V. K., Potsdam, M. A., Jain, R., Bauer, A., and Strawn, R.: Recent Advancements in the Helios Rotorcraft Simulation Code, in: 54th AIAA Aerospace Sciences Meeting, p. 0563, San Diego, CA, <https://doi.org/10.2514/6.2016-0563>, 2016.
- Wissink, A. M., Jayaraman, B., Tran, S. A., Jain, R., Potsdam, M. A., Sitaraman, J., Roget, B., and Lakshminarayan, V. K.: Assessment of Rotorcraft Download Using Helios v8, in: 2018 AIAA Aerospace Sciences Meeting, p. 0026, Kissimmee, FL, <https://doi.org/10.2514/6.2018-0026>, 2018.
- Yeo, H., Bosworth, J., Acree Jr, C., and Kreshock, A. R.: Comparison of CAMRAD II and RCAS Predictions of Tiltrotor Aeroelastic Stability, *Journal of the American Helicopter Society*, 63, 1–13, <https://doi.org/10.4050/JAHS.63.022001>, 2018.
- Yonekura, K. and Suzuki, K.: Data-Driven Design Exploration Method using Conditional Variational Autoencoder for Airfoil Design, *Structural and Multidisciplinary Optimization*, 64, 613–624, <https://doi.org/10.1007/s00158-021-02851-0>, 2021.